A FOREST ENTOMBED IN ICE: A UNIQUE RECORD OF MID-HOLOCENE CLIMATE AND ECOSYSTEM CHANGE IN THE NORTHERN ROCKY MOUNTAINS, USA

by

Daniel Kent Stahle

A thesis submitted in partial fulfillment
of the requirements for the degree

of

Master of Science

in

Earth Sciences

MONTANA STATE UNIVERSITY
Bozeman, Montana

May 2022

ACKNOWLEDGEMENTS

Thank you, Dr. Gregory Pederson, for providing exceptional guidance and support over the past several years. Your mentorship has greatly impacted my life for the better. You have helped me to improve the way I approach scientific questions, efficiently collect meaningful data, and greatly advanced my writing skills along the way. Dr. Dave McWethy, thank you for your support through my academic pursuit of this degree and the development of this project. I have learned a great amount from you both in the classroom and in the field. Dr. Mark Skidmore, thank you for your participation as an advisor on my committee, your expertise and contributions improved the way I approached this project.

TABLE OF CONTENTS

LIST OF FIGURES

LIST OF FIGURES – CONTINUED

LIST OF TABLES

ABSTRACT

Across the high alpine of the northern Rocky Mountains small vestiges of perennial ice have endured for thousands of years. These ice patches reside hundreds of meters above modern treeline, with some persisting through mid-Holocene warmth and others establishing at the onset of a cooler period that began around 5,000-5,500 years BP. Recent warming-driven melting at the margins of one ice patch high on the Beartooth Plateau of northern Wyoming exposed over 30 intact mature whitebark pine (*Pinus albicaulis*) tree boles, all > 25 cm in diameter. We extracted cross-sectional samples from the stems of 27 preserved logs, and radiocarbon dated annual growth rings from 11 of these trees, anchoring the chronology to a date range spanning 5,947 to 5,436 years BP ± 51.3 years. From this fossil wood chronology, we developed estimates of warm-season, annual, and biennial average temperatures for upper-elevation treeline during the mid-Holocene. To identify the predominant climate-growth relationships of the subfossil trees, we sampled live whitebark pine trees growing at an adjacent treeline site approximately 120 m lower in elevation. Temperature was found to be the major driver of variability in tree growth at the modern treeline location, with trees producing narrower (wider) rings during periods of cooler (warmer) growing season temperatures. Using linear and non-linear transfer functions based upon the stable statistical relationship between modern tree growth and temperature, we reconstructed past temperature estimates from the ice patch subfossil ring-width chronology. Our results provide estimates of mid-Holocene warm-season (and biennial) average temperatures ranging from 5.7-6.5 °C (-0.44-0.26 °C) respectively. A multi-century regional cooling trend beginning around 5,650 years BP resulted in average temperatures declining below a warm-season (biennial) critical threshold of ~5.8 °C (-0.34 °C), likely leading to the eventual death of the whitebark pine stand and subsequent formation of the ice-patch. This high-quality paleo-ecological dataset reveals a major shift in the alpine and forest ecotone on the Beartooth Plateau following the mid-Holocene warm period and offers further insight on the thermal limits of whitebark pine trees in the Greater Yellowstone Ecosystem.

INTRODUCTION

Ice patches have resided well above the modern upper treeline and have persisted on the landscapes of the Northern Rocky Mountains for thousands of years. Many of these perennial ice features established at a time when the Northern Hemisphere began to cool following the mid-Holocene warm period, a transitional period between 5,000-6,000 years ago. Over the ages, layers of snow transformed to ice, trapping proxies of environmental change including sediments, pollen, charcoal, and incorporating atmospheric chemical signatures between the frozen lenses. These ice-patches also hold animal remains, tools, and artifacts used by Indigenous peoples, and even complete trees that would have disintegrated millennia ago, but instead, were encased in ice and preserved for centuries. Due to recent anthropogenic warming, the margins of many of these ice-patches are melting, exposing artifacts and tree boles to the harsh weathering of high-elevation, alpine environments.

In 2016 we extracted cross-sectional samples from the stems of 27 individual whitebark pine (*Pinus albicaulis*) exposed on the margins of the Tolman ice-patch high on the Beartooth Plateau of Northern Wyoming. Using dendrochronological methods, we crossdated all 27 of the sampled trees and combined their ring-width series into a floating chronology spanning a range of radiocarbon dates between 5,947-5,436 ± 51.3 cal. years BP. Analysis of climate and stand-growth relationships of living whitebark pine trees growing adjacent to the ice patch show great sensitivity to temperature, allowing for transfer functions to be used in reconstructing warm-season, annual, and biennial average temperature over the mid-Holocene period from the subfossil whitebark pine tree-rings. The chronology statistics of this collection of subfossil wood indicate great sensitivity to temperature, with declining growth rates near the end of the record, coinciding with tree-ring reconstructed regional cooling and the formation of the ice-patch in which the tree boles are preserved.

CHAPTER TWO

A FOREST ENTOMBED IN ICE:
A UNIQUE RECORD OF MID-HOLOCENE CLIMATE AND ECOSYSTEM CHANGE IN THE NORTHERN ROCKY MOUNTAINS, USA

Contribution of Authors and Co-Authors

Manuscript in Chapter 2

Author: Daniel Stahle

Contributions: Conceptualization, Investigation, Data production, Formal analyses, Methodology, Visualization, Writing – original draft

Co-Author: Gregory Pederson

Contributions: Conceptualization, Investigation, Formal analyses, Methodology, Visualization, Resources, Writing – review & editing

Co-Author: David McWethy

Contributions: Investigation, Visualization, Resources, Writing – review & editing

Co-Author: Nickolas Kichas

Contributions: Writing – review & editing

Co-Author: Craig Lee

Contributions: Conceptualization, Resources, Writing – review & editing

Co-Author: Nathan Chellman

Contributions: Conceptualization, Resources, Writing – review & editing

Co-Author: Joseph McConnell

Contributions: Conceptualization, Resources, Writing – review & editing

Manuscript Information Page

A Forest Entombed in Ice: A Unique Record of Mid-Holocene Climate and Ecosystem Change in the Northern Rocky Mountains, USA.

Daniel Stahle, Gregory Pederson, David McWethy, Nickolas Kichas, Craig Lee, Nathan Chellman, and Joseph McConnell

Quaternary Science Reviews

Status of Manuscript:
__X__Prepared for submission to a peer-reviewed journal
______Officially submitted to a peer-reviewed journal
______Accepted by a peer-reviewed journal
______Published in a peer-reviewed journal

A Forest Entombed in Ice: A Unique Record of Mid-Holocene Climate and Ecosystem Change in the Northern Rocky Mountains, U.S.A.

Daniel Stahle[1,2], Gregory Pederson[1], David McWethy[2], Nickolas Kichas[2], Craig Lee[3], Nathan Chellman[4], Joseph McConnell[4]

[1]U.S. Geological Survey, Northern Rocky Mountain Research Station - Bozeman, Montana, United States.
[2]Montana State University - Bozeman, Montana, United States.
[3]Institute of Arctic and Alpine Research, University of Colorado - Boulder, Colorado, United States.
[4]Division of Hydrologic Science, Desert Research Institute, United States.

ABSTRACT

Across the high alpine of the northern Rocky Mountains small vestiges of perennial ice have endured for thousands of years. These ice patches reside hundreds of meters above modern treeline, with some persisting through mid-Holocene warmth and others establishing at the onset of a cooler period that began around 5,000-5,500 years BP. Recent warming-driven melting at the margins of one ice patch high on the Beartooth Plateau of northern Wyoming exposed over 30 intact mature whitebark pine (*Pinus albicaulis*) tree boles, all > 25 cm in diameter. We extracted cross-sectional samples from the stems of 27 preserved logs, and radiocarbon dated annual growth rings from 11 of these trees, anchoring the chronology to a date range spanning 5,947 to 5,436 years BP ± 51.3 years. From this fossil wood chronology, we developed estimates of warm-season, annual, and biennial average temperatures for upper-elevation treeline during the mid-Holocene. To identify the predominant climate-growth relationships of the subfossil trees, we sampled live whitebark pine trees growing at an adjacent treeline site approximately 120 m lower in elevation, or based on modern estimated lapse rates, ~1.3 °C (annual average) warmer than the ice patch preserved treeline site. Temperature was found to be the major driver of variability in tree growth at the modern treeline location, with trees producing narrower (wider) rings during periods of cooler (warmer) growing season temperatures. Using linear and non-linear transfer functions based upon the stable statistical relationship between modern tree growth and temperature, we reconstructed past temperature estimates from the ice patch subfossil ring-width chronology. Our results provide estimates of mid-Holocene warm-season (and biennial) average temperatures ranging from 5.7-6.5 °C (-0.44-0.26 °C) respectively. A multi-century regional cooling trend beginning around 5,650 years BP resulted in average temperatures declining below a warm-season (biennial) critical threshold of ~5.8 °C (-0.34 °C), likely leading to the eventual death of the whitebark pine stand and subsequent formation of the ice-patch. This high-quality paleo-ecological dataset reveals a major shift in the alpine and forest ecotone on the Beartooth Plateau following the mid-Holocene warm period and offers further insight on the thermal limits of whitebark pine trees. The record also provides new insights into the climatic conditions favorable for ice patch development and persistence in the Greater Yellowstone Ecosystem, as well as the near-term expectation that this ice patch, as well as many other GYE ice patches, are likely to disappear within decades with continued warming.

HIGHLIGHTS

- We identified 30 mature whitebark pine trees emerging from the margins of an ice patch located ~120 meters above the modern treeline, a subset of these tree boles provide radiocarbon dates anchoring the chronology to a date range of 5,947 to 5,436 years BP ± 51.3 years.

- Modern day whitebark pine trees growing adjacent to the ice patch show significant sensitivity to temperature allowing for transfer functions to be used in reconstructing warm-season, annual, and biennial average temperature over the mid-Holocene period preceding ice patch formation.

- Based on the transfer function results, the subfossil trees established during the end of the early/mid-Holocene warm period, when warm-season (biennial) average temperatures were ~6.21 °C (-0.03 °C).

- The subfossil trees record a multi-century regional cooling trend beginning around 5,650 years BP that resulted in average temperatures declining below a warm-season (biennial) critical threshold of ~5.8 °C (-0.34 °C), leading to the eventual death of the whitebark pine stand and subsequent formation of the ice-patch.

1. INTRODUCTION

Across high-elevation alpine landscapes of the northern Rocky Mountains (hereafter NRM), small vestiges of perennial ice have persisted for thousands of years. Unlike glaciers, these ice patch features do not accrete sufficient mass to move under their own weight, therefore they do not ablate ice through glacial processes or erode their underlying bedrock (Glen, 1955; Meulendyk et al., 2012). Instead, these ice masses accumulate in layers and preserve subaerially deposited materials, such as pollen, animal dung, and charcoal, within their frozen layers, as well as biological materials beneath the stable ice mass that predate establishment of the ice (Chellman et al. 2021). These ice patches reside hundreds of meters above modern treeline, with some persisting through the early/mid-Holocene warm period (ca. 12,000-5,500 years BP) and others establishing at the onset of a cooler period that began around 5,000-5,500 years BP (Bader et al., 2020; Lee and Puseman, 2017; Marcott et al., 2013). As global average temperatures have become warmer, particularly over the past few decades, ice patches have been in a phase of negative mass balance, revealing organic materials that were previously entombed and would have disintegrated millennia ago if not for the preserving effect of the ice. Melting around the margins of these ice patches has exposed human-made cultural and biological materials, findings that have mobilized significant research under the archeological subdiscipline known as ice patch archeology (Dixon et al., 2014; Hare et al., 2012; Lee, 2010, 2018; Lee and Puseman, 2017; Reckin, 2013). In addition to artifact preservation, ice cores retrieved from these ice patches contain valuable information on vegetation and climate and have provided insight on changing environmental conditions over thousands of years (Chellman et al., 2017, 2021).

During an archeological survey of ice patches on the Beartooth Plateau in the summer of 2015, over 30 preserved large (>25 cm) tree boles were discovered melting out of the margin of the Tolman ice patch on the Beartooth Plateau, located east of Yellowstone National Park in the Shoshone National Forest of northwest Wyoming (Figure 1) (Lee and Puseman, 2017). The trees at the site were identified as whitebark pine (*Pinus albicaulis*) (hereafter WBP) due to the combination of nearby modern stands, along with evidence from general wood anatomy exhibiting dimpling from rays between annual rings (Kellogg et al. 1982, Hoadley 1990) - an anatomical diagnostic that separates WBP from the physiologically similar species limber pine (*Pinus flexilis*). We classify these remnant logs as 'subfossil' referring to nonlithic wood material that postdates the Pleistocene epoch and still contains carbon (Roig et al., 2001). The discovery of these trees emerging from the ice patch was particularly striking because they were found ~120 m above current day treeline. Their presence raises important questions about the prevailing climatic conditions that existed when their establishment took place as well as the sequence of events leading to their demise and eventual entombment in the ice patch.

Whitebark pine trees growing at or near upper treeline often exhibit growth patterns that are strongly controlled by warm-season temperature conditions and, in some cases temperatures across more than one growing season due to lagged physiological processes (e.g., carbon storage) (Bunn et al. 2018; Körner & Paulsen, 2004). In WBP along with other members of the 5-needle pine genera, moisture sensitivity has also been shown at sites located within several hundred meters below treeline and on warm dry aspects where the soils are well drained (Kipfmueller and Salzer 2010) (Bunn et al. 2011). In addition to moisture and temperature limited growth, recent research has also shown that snowpack can serve as the dominant growth controlling factor across a range of high-elevation species by limiting growing season length and through direct energy limitation (Pederson et al. 2011b, Pederson et al. 2013, Coulthard et al. 2020). With careful investigation of the modern WBP growth-climate relationship, relative to the growth record of subfossil tree-rings recovered from the Tolman ice patch, it may be possible to generate a multi-century, mid-Holocene record of either temperature, snowpack, or moisture variability just prior to the formation of the modern ice patch. To accomplish this central research goal, we ask: 1) What are the dominant climate controls on WBP tree growth at the modern upper treeline site?; 2) are the linear (or non-linear) relationships between climate and tree growth statistically robust enough that a transfer function could be utilized to estimate mid-Holocene climatic conditions from the sub-fossil WBP chronology?; and 3) What were the mid-Holocene prevailing climate conditions and trends that enabled expansion and then contraction of upper treeline forests just prior to formation and growth of the ice patch?

1.1 Holocene Temperature Records for North America

Global reconstructed temperature records exhibit varying trends throughout the Holocene period, with some proxy records showing warming over the entire Holocene, while others show warming followed by late-Holocene cooling (Liu et al. 2014, Marcott et al. 2013; Marsicek et al. 2018). These differing patterns of warming and cooling in global temperature reconstructions and proxy records became known as the "Holocene temperature conundrum" (Liu et al. 2014; Bader et al. 2020). Recent work by Bader et al. (2020) document these regionally specific modes of annual warming and cooling trends in a transient climate model run over the last 8,000 years. This high-resolution, mid-Holocene-to-present model was the first to include the effect of changing aerosols, landcover, and sea-ice forcings on regional climate patterns and trends. Results show sustained warming of annual average temperatures centered over the tropics and sub-tropics, while mid- to high-latitude regions, from 30 °N poleward, exhibit gradual cooling trends that accelerate around 4,000 years BP. Most relevant to this work, Bader et al. (2020; see Figs. 2 and 3) show a strong region of cooling centered over the western U.S. from the mid to late-Holocene, driven by increasing Arctic summer sea-ice concentration and decreasing summer high-latitude solar radiation.

The most recent high-elevation and Holocene-length climate record for the region was generated from a nearby (within ~5 km) ice patch stable water isotope ($\delta^{18}O$) record from a well-dated ice core chronology (Chellman et al. 2021). The authors interpreted the isotopic record as a combined indicator of cool-season moisture and temperature for the broader Beartooth Plateau. In addition to the isotope record, estimates of ice accumulation rates through time were used as a qualitative indicator of cool-season moisture and temperature. Taken together, the proxies derived from this ice patch record show generally cool- and wet-cool-season conditions through the early Holocene, with a period of warmth centered on 4,100 years BP followed by rapid cooling over subsequent millennia (Chellman et al. 2021). The subfossil WBP chronology recovered from the Tolman ice patch provides an opportunity to develop a warm-season focused climate proxy that may inform changing high-elevation climate conditions centered within the modeled western U.S. regional cooling trend shown by Bader et al. (2020), and for a period of regional ice patch formation and growth, upper treeline elevation reductions, and regional lake level increases (Chellman et al. 2021; Shuman et al. 2017; Lee and Puseman, 2017).

Previous studies have developed ‘floating’ tree-ring chronologies (i.e. not absolutely dated) from various anoxic sedimentary preservation media such as permafrost, peat bogs, volcanoclastic debris deposits, and petrified wood (Edvardsson, 2016; Grudd et al., 2002; Roig et al 2001; Wright et al., 2016), while stable isotope analysis of ancient tree-ring material has been used to estimate climatic conditions during the Pliocene and Eocene (Ballantyne et al., 2006; Jahren and Sternberg, 2003). For instance, Csank et al. (2012) developed a ~100-year floating tree-ring chronology of larch (*Larix* spp.) from the late Pliocene-early Pleistocene (2.4-2.8 Ma). However, while wood debris and wooden artifacts have been recovered from ice patches in the broader Rocky Mountain range (Benedict et al., 2008; Lee and Puseman, 2017), high resolution dendrochronological records from time periods predating the last 5,000 years are scarce globally, and non-existent in the NRM region (International Tree Ring Data Bank, National Oceanic and Atmospheric Association; https://www.ncdc.noaa.gov/paleo/treering.html) (Brown, 1996; Salzer et al. 2014).

The primary objectives of this study are to first reconstruct mid-Holocene, high-elevation climate at a time of rapid regional climate and ecosystem change from a floating subfossil WBP chronology; and second, to disentangle the conditions and sequence of events leading to the establishment of the WBP trees above current treeline and their eventual demise and entombment in the ice patch. To accomplish these objectives we: 1) develop crossdated tree-ring chronologies for the ice patch trees and at a nearby modern WBP treeline site, 2) establish climate-growth relationships using the modern treeline forest chronology, 3) utilize linear and non-linear transfer functions, based on modern growth-climate relationships, to develop palaeothermometry estimates of mean warm-season, annual, and biennial temperature from the subfossil WBP chronology to estimate mid-Holocene, high-elevation climate conditions, and 4) interpret the temperature reconstructions for the mid-Holocene to better understand the conditions under which the WBP trees established, died, and the ice patch developed.

2. MATERIALS & METHODS

To accomplish our central study goals, we first produced a crossdated WBP tree-ring chronology assigned to an arbitrary calendar year from 28 subfossil tree cross-sections sampled after recently emerging from the Tolman ice patch. The crossdated chronology was next anchored in time using radiocarbon dates from individual annual rings sampled from 11 trees. The climate variables (i.e., average temperature, accumulated snowpack, total precipitation) and seasons selected for reconstruction were identified using climate-growth relationships from a nearby upper treeline modern WBP chronology (Figure 1). The strongest and statistically most robust climate-growth relationships were identified for the average temperature variable over 6-, 12-, and 24-month optimal seasonal windows using '*seascorr*" - seasonal partial correlation analysis (Meko et al. 2011). Finally, we develop linear and non-linear transfer functions from the optimized modern WBP temperature-growth relationships, which were then applied to the subfossil WBP chronology to generate multi-century estimates of high-elevation mean temperature variability and trends. Linear and non-linear transfer functions were explored for the average temperature reconstructions since the subfossil chronology exhibits slower growth and reduced variability relative to the modern treeline WBP chronology (Figure S1). This implied that all the predictions of past temperature would be made from one end of the temperature-growth distribution, so the shape of the relationship and prediction quality at the ends of the distributions needed be assessed and utilized to bound a range of past temperature estimates. We tested the robustness of our transfer functions, estimated prediction errors, and selected the best seasonal climate reconstruction target with the lowest prediction error across the range of observations and extremes using a boot-strapped k-folds cross-validation method, and a Central-Edge test (Jevšenak et al., 2018; Jevšenak and Levanič, 2018). We then interpret the optimized warm-season to biennial average temperature reconstructions for the mid-Holocene within the context of the Tolman ice patch and ecological changes influencing treeline establishment as well as other climate model and proxy-based paleoclimatic interpretations for the region.

2.1 Tolman Ice Patch

The Tolman ice patch (located at approximately 44°57'44"N, 109°23'38"W) resides in the uppermost headwaters of Bennett Creek, a tributary of the Clarks Fork of the Yellowstone River watershed (Figure 1). This drainage is located on the eastern edge of the Beartooth Plateau, an orographic feature that is part of the broader Yellowstone crescent of high terrain. The Plateau collects an abundance of winter precipitation from storm tracks off the Pacific that funnel up the Snake River Plain, and a spring (May-Jun) season precipitation pulse generated from easterly upsloping moisture advected from the Gulf of Mexico (Licciardi, J.M., 2008; Wise et al., 2018). The annual temperature at the ice patch site averages -1.0 °C (Table 1) over 1900 to 2018, and snowpack as estimated from the nearby, lower elevation (2853 m) SNOTEL located 16 km to the west at Beartooth Lake site reaches a median of 63.2 cm, on the median peak SWE (snow water equivalence, 1991-2020) date of May 7th and a median melt out date of June 27th over the same period (NRCS National Water and Climate Center | SNOTEL Data & Products (usda.gov)). The ellipsoidal ice patch is situated on a northeast aspect ~120 m above treeline at 3,091 m elevation and measures around 200 m along its north-south long axis, with a maximum width of 105 m along the east-west short axis. The ice patch is oriented on the landscape below a convex topographic low, or nivation hollow, and east of a ridge, where wind-blown snow from the west is preferentially deposited on the lee side of the ridge during winter months. The unique orientation of the ice patch on the landscape results in several meters of additional snow overlying the ice patch in the spring. Over time, during the right temperature conditions, the localized accumulation of snow transforms into self-insulating layered ice, allowing the ice patch to persist through the summer warm seasons (Chellman et al., 2021; Meulendyk et al., 2012). However, the ice patch does not accumulate enough mass to deform or move downslope and thus does not physically erode the underlying bed, as evidenced by the orientation of layered ice, the intact and partially rooted-in-place WBP boles, and the absence of glacial erosional features like scoured substratum or depositional moraines (Glen, 1955).

The subfossil WBP tree boles were discovered melting out of an area along the margin of the southeast quadrant of the ice patch. The WBP stems show no sign of damage or growth disturbance from avalanching and a comprehensive survey of their outer surfaces revealed only one *J*-shaped beetle gallery out of the remnants of 30 different individual trees. This finding confirms the presence of bark beetles (most likely *Dendroctonus* spp.) in the area over 5,400 years BP, but a single gallery along with a lack of fungal blue-staining preserved on any of the cross-sections is not suggestive of extensive insect-related mortality. The intact condition of the WBP logs progressively diminishes with distance from the ice patch margin suggesting that, as the ice patch shrinks in size, more wood material is being exposed to the seasonally harsh weathering and common freeze-thaw cycles of the high plateau, which results in relatively rapid deterioration of the wood.

2.2 Modern Upper Treeline Site

To identify the environmental factors that limit modern WBP tree growth at its upper elevational extent, we sampled living WBP trees growing in the adjacent upper treeline, approximately 120 m below the ice patch (Figure 1). Warm-season (May-Oct) and annual (Jan-Dec) temperature at the upper treeline site averaged 7.1 °C and 0.3 °C, respectively from 1900-2018 (Table 1). The treeline forest site is largely undisturbed, showing no sign of logging and limited historical use. Treeline in this part of the Beartooth plateau is not abrupt but rather a diffuse transitional zone that varies with elevation and topography. These high-elevation environments, where the physiology of WBP ranges from full growth forms (>25 cm diameter at breast height; DBH) to stunted krummholz that self-insulate just above the ground surface, are characterized by a combination of physiological stressors that limit tree growth, reduce biomass gain, and restrict regeneration (Harsch and Bader, 2011). Temperature differences between the WBP forest site and the ice patch were calculated based on the dry adiabatic lapse rate, providing a consistent seasonal and annual estimate of ~1.3 °C difference in temperature (Table 1).

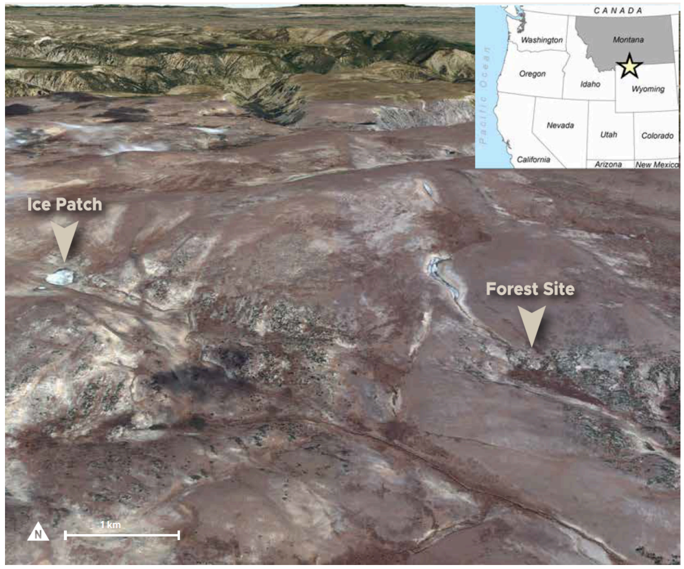

Figure 1. Map of the ice patch and contemporary forest site on the Beartooth Plateau in northwestern Wyoming, United States. Subfossil whitebark pine trees were sampled at the ice patch, while living whitebark pine trees were sampled at the modern forest treeline site, approximately 3 km to the southeast and 120 m below in elevation.

Table 1. Temperature (°C) estimates from the modern forest and ice patch sites as well as temperature difference between sites estimated over years 1900-2018. Temperature estimates for the ice patch and forest site were interpolated from the Parameter-elevation Regressions on Independent Slopes Model (PRISM) dataset using inverse-distance squared weighting from surrounding grid points and were grouped into four seasonal windows for analysis.

Seasonal Window	**Forest Site (°C)**	**Ice Patch (°C)**	**Difference (°C)**
Warm-season (*May - October*)	7.07	5.79	1.27
Annual (*January - December*)	0.32	-0.99	1.31
Optimized Annual (*Previous March - January*)	1.11	-0.19	1.31
Optimized Biennial (*Previous January - October*)	0.95	-0.36	1.30

2.3 Field Sampling and Sample Preparation

Cross-sectional samples were extracted from 27 intact subfossil WBP tree boles melting out of the margin of the ice patch. At the adjacent upper forest treeline site, we extracted 32 increment cores from 16 living WBP trees (two cores per tree) of similar diameter (> 25 cm DBH) and upright growth form (i.e., non-krummholz) to the stems of the subfossil logs recovered from the ice patch. Cross-sections and core samples were mounted and sanded to a fine polish to expose the minute anatomy of each annual growth ring. All samples were examined using a binocular microscope and classic dendrochronological methods were used to separately crossdate the tree-rings for both the subfossil ice patch and forest site WBP collections (Douglass, 1941; Stokes & Smiley, 1996). The tree-rings were measured using a sliding stage micrometer with a precision of 0.001 mm and the ring-width measurements were submitted to the dating quality control program COFECHA for statistical verification (Holmes, 1983).

To assess the shared variability in tree growth and growth-climate relationships for both the subfossil and modern WBP collections, we utilized the raw ring-width measurements as well as a standardized, unitless ring-width index (RWI). For the raw ring-width chronology, each tree-ring measurement series was individually edited to remove the biological trends associated with juvenile tree growth along with any obvious ecological disturbance registered in the tree-rings to produce a "quality controlled" (QC) measurement series. Doing so enabled us to avoid detrending and transforming the raw ring-width data into unitless indices, preserving the measurement values (mm units) for each tree-ring series. This was critical for the construction of growth-climate transfer functions (described below) since preservation of the mean and distribution of the raw growth is required to capture potential mean changes in reconstructed climate based on the subfossil wood record.

To assess the quality of the retained climate signal in the modern raw WBP tree-ring chronology, a conservatively detrended version of the record was produced for use in monthly and seasonal correlation analyses. We conservatively detrended each series by fitting either a negative exponential curve, negative regression, or mean line to remove the geometric growth trend (Fritts 1976). The resultant series were then standardized by dividing by the fitted trend line, transformed into unitless ratio (index), and then combined into a composite chronology by calculating the weighted mean across all samples (Cook and Peters 1997). We computed the average raw and standardized ring-width chronologies using the "*dplR*" package (version 1.7.2) (Bunn 2008) in the statistical program R (version 4.0.5) (R Development Core Team 2008). In both chronologies, only the period of record where the express population signal remains above 0.85 was retained for use in analyses, limiting additional error attributable to decreasing sample number through time to < 15% (Wigley et al., 1984).

2.4 Radiocarbon Sampling of Subfossil Tree-rings

We extracted approximately 0.5-2.0 g of wood material from the individual growth rings of 11 subfossil WBP cross-sections included within the arbitrarily crossdated floating tree-ring chronology. These 11 growth ring samples were submitted to the National Ocean Sciences Accelerator Mass Spectrometry Lab (NOSAMS) at the Woods Hole Oceanographic Institution for ^{14}C radiocarbon dating. Radiocarbon dates were calibrated using the "*intcal20*" curve within the R program using the Bayesian radiocarbon chronology package "*Bchron*" (Haslett and Parnell 2008).

2.5 Climate Analyses

Climate data for the study sites, from the period of 1900-2018, were obtained from the Parameter-elevation Regressions on Independent Slopes Model (PRISM) at 4 km spatial resolution using the AN81m version of the dataset (Daly et al. 2008). Point estimates of surface temperature and precipitation histories at the locations of the ice patch and modern forest sites were generated using inverse-distance squared weighting from surrounding grid points for each site elevation, as estimated from the underlying digital elevation model the PRISM product is based upon. To test for possible inhomogeneities and trend departures in our climate time series, we compared correlations and trends in the monthly, annual, and seasonal temperature and precipitation data from the PRISM dataset with the TerraClimate dataset, which is an alternative high-resolution ~4 km monthly climate and water balance model spanning 1958-2015

(Abatzoglou et al., 2018). Annual variability and trends in climate between the two datasets over the 1958-2015 common interval were strongly, positively correlated ($r > 0.98$, $p < 0.001$), indicating a lack of significant temporal bias from one dataset over the other, so we opted to use the PRISM data in all further analyses due to the greater time coverage (1900-2018). Basin-scale and individual station snow water equivalence (SWE) data were obtained from observational records collected by the Natural Resource Conservation Service's SNOTEL stations and snow course sites located within the basin (Pederson et al., 2013; Pederson et al., 2011; Wise et al. 2018).

We used the "*seascorr*" function in the "*treeclim*" (Zang & Biondi, 2015) and "*dendroTools*" (Jevšenak et al., 2018; Jevšenak and Levanič, 2018) R software package, as well as correlation and regression analyses, to investigate seasonal relationships between tree growth (both raw mm ring-widths and the standardized ring-width index), precipitation (mm), temperature (°C), and snowpack (measured as April 1 SWE) (Zhang and Biondi, 2015). The "*seascorr*" function was used to identify periods of time within 6-, 12-, and 24-month windows exhibiting the strongest relationships between live WBP tree growth and our different climate metrics. Using these optimized response windows, we were able to identify four ideal seasonal targets for climate reconstructions from the subfossil tree-ring chronology: (1) warm-season (May-Oct), (2) annual (Jan-Dec), (3) optimized annual (Mar of the previous year through Jan of the current year) and (4) optimized biennial (Jan of the previous year through Oct of the current year; supporting information Figure S3). We also investigated climate-growth relationships at an adjacent high-elevation WBP chronology (Grass Mountain: GRM) to add samples to our growth data analyses, but discovered that trees at GRM exhibited different seasonal climate-growth relationships and were therefore excluded from our analyses.

2.6 Transfer Function Construction and Model Cross-Validation Methods

Following similar methods reported by Csank et al. (2011, 2013) we constructed transfer functions to reconstruct past temperature from the subfossil WBP chronology, using the contemporary relationship between tree growth and temperature across the four seasonal windows that were identified through "*seascorr*" partial correlation analysis. We developed and tested the influence of both linear and non-linear relationships between temperature and tree growth on prediction quality. We utilized least-squares linear regression (*MLR*), and artificial neural networks with the Bayesian regularization training algorithm (*BRNN*), through the "*dendroTools*" package to explore both linear and non-linear relationships between temperature and tree growth. As described in Jevšenak et al, (2018) the "*brnn*" function in "*dendroTools*" fits a two-layer neural network that uses the Nguyen and Widrow algorithm to assign initial weights and the Gauss-Newton algorithm to perform the optimization (Foresee and Hagan, 1997; MacKay, 1992; Nguyen and Widrow, 1990). We tested the statistical prediction accuracy and compared the quality of seasonal to biennial average temperature reconstructions resulting from the linear and non-linear regression methods using bootstrapped 10-fold cross-validation, also known as k-fold cross-validation, whereby 10 random observations were withheld from the model calibration and then compared against model predictions for 100 iterations (Jevšenak et al., 2018). To assess the prediction accuracy across the range of predicted values, a subset of the extreme (edge) data points were estimated as validation data using a central-edge test (Jevšenak et al., 2018). Model performance was evaluated using a variety of metrics, including correlation coefficient (r), root mean square error ($RMSE$), root relative squared error ($RRSE$), index of agreement (d), reduction of error (RE), coefficient of efficiency (CE), and mean bias (Jevšenak et al., 2018).

3. RESULTS

3.1 Radiocarbon Dating of Subfossil Whitebark Pine Chronology

An arbitrarily dated floating tree-ring chronology spanning 512 years was compiled from the subfossil WBP cross-sections (TOL; series intercorrelation $r = 0.56$ $p < 0.001$; Figure 2A, Table 2), while a mean ring-width chronology spanning 1620-2018 (399 years) was compiled from the modern WBP increment cores (TAL; series intercorrelation $r = 0.52$; $p < 0.001$; Figure 2B, Table 2). The floating TOL subfossil chronology was anchored to calendar years before present (BP) using the linear relationship from least squares regression between the calibrated median radiocarbon dates from the individual crossdated growth rings assigned to an arbitrary calendar year (Figure 3). The relative location of the radiocarbon dated tree-rings fit a similar distribution in time as the arbitrary chronology, supporting both the accuracy of the subfossil tree-ring chronology crossdating and the quality of the radiocarbon dates. The final calibrated WBP chronology spans a date range of 5,947 to 5,436 calendar years BP ± 51.3 years.

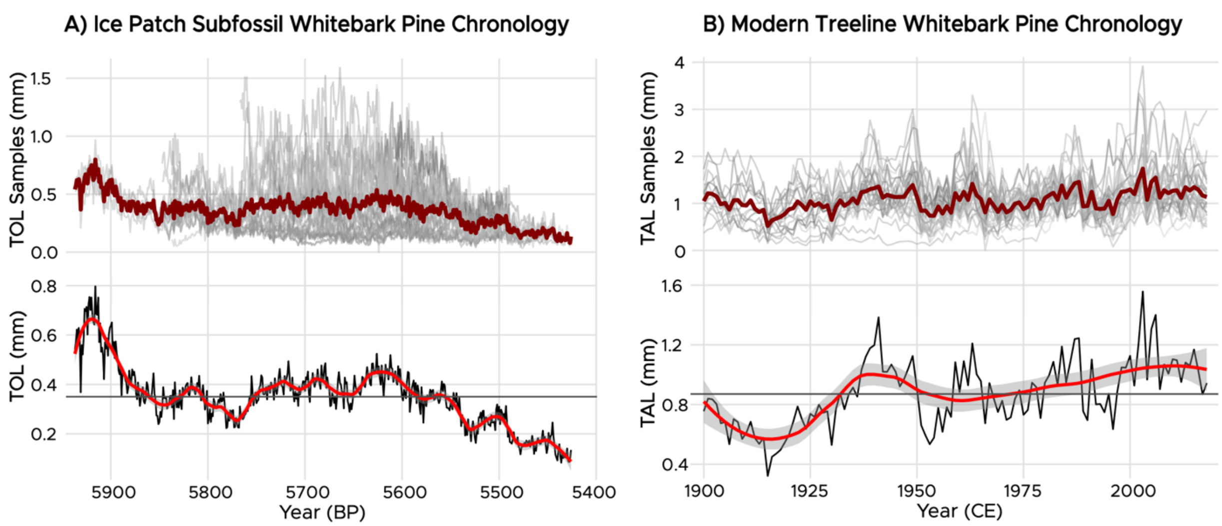

Figure 2. Tree-ring-width measurements were combined and average raw ring-width chronologies were computed for both the subfossil (*A*) and modern (*B*) whitebark pine (*Pinus albicaulis*) tree-ring-width chronologies with a 50-year smoothing spline (red line) TOL = subfossil WPB specimens collected from the Tolman ice patch and TAL = modern upper treeline WPB chronology. *Top plots*: the raw mm ring-widths and the raw average growth chronology for the stand (red line). *Bottom plots*: raw average growth chronology for the stand (mm) with a 50-year smoothing spline (red line w/ gray 95% confidence bar).

Table 2. Tree-ring data for whitebark pine (*Pinus albicaulis*) sampled from subfossil wood melting out of the margins of an ice patch high on the Beartooth plateau of northern Wyoming (TOL) and from live whitebark pine trees sampled at an adjacent upper treeline site (TAL).

	Subfossil Chronology (TOL)	Modern Chronology (TAL)
No. of Dated Series	50	32
Series Timespan	512 years (floating)	399 years (1620-2018)
Series Mean Length	247 years	149 years
Series Intercorrelation	0.552	0.521
Avg. Mean Sensitivity	0.166	0.236
Max Ring-widths (mm)	0.524	1.558
Mean Ring-widths (mm)	0.325	0.871
Min Ring-widths (mm)	0.083	0.321

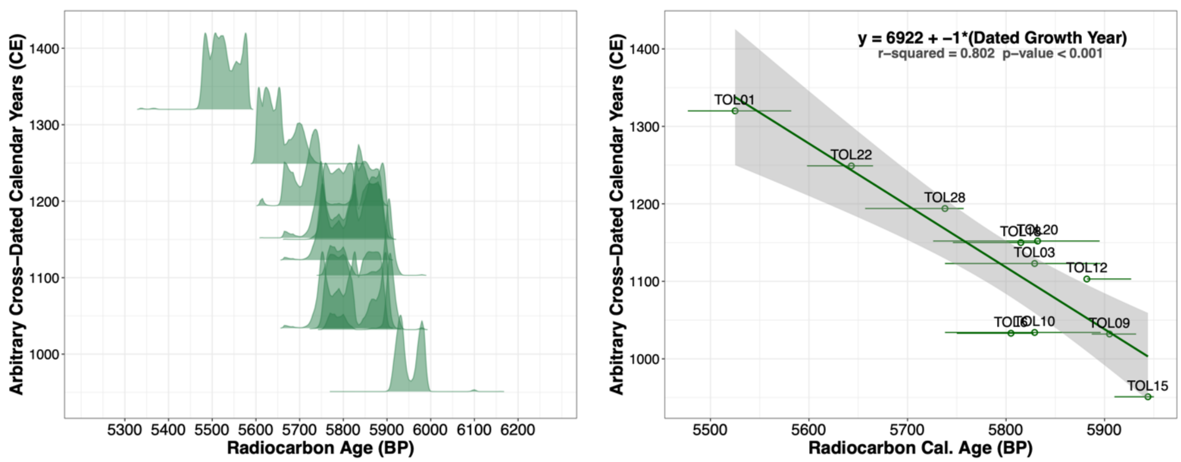

Figure 3. (*Left*) Calibrated radiocarbon age distributions plotted against crossdated growth rings from 11 different subfossil trees. (*Right*) The subfossil chronology was anchored using the linear relationship between the calibrated median radiocarbon dates from material extracted from individual growth rings (circles) plotted against and the arbitrary years assigned to the same tree-ring material sampled for radiocarbon dating, bracketed with 95% confidence intervals (gray shading).

3.2 Climate Response of Living Whitebark Pine Trees

We found temperature (°C) to be the dominant control on WBP tree growth at the modern upper treeline site (Figure 4). Specifically, WBP tree growth is consistently, positively associated with temperature over every month and season of the year, with the strongest relationship occurring between tree growth (raw mm ring-widths) and annual average temperature ($r = 0.44$; $p < 0.001$; Figure 4). The TAL raw ring-width chronology showed consistently higher correlations with temperature than the detrended and standardized tree-ring indices (TAL.std) over all seasonally averaged time intervals [annual (Jan-Dec), warm (May-Oct), spring (Mar-May), summer (Jun-Aug)] (Figure 4). Note the differing growth-climate response shown in Figure 4 for the nearby Grass Mountain (GRM) WBP raw (GRM.raw) and standard (GRM.std) chronologies, which precluded it from inclusion in further analyses.

Whitebark pine tree growth was also found to be negatively correlated with snowpack ($r = -0.35$, $p < 0.05$; supporting information Figure S2). The positive relationship of tree growth to temperature and negative relationship with snowpack suggests that, in these high-elevation environments, growth is favored when conditions are warmer with relatively less snow on the ground. However, temperature also directly influences snowpack, with snowpack accumulating and persisting under cooler temperatures and ablating under warmer temperatures (e.g., Barnett et al., 2008; Pederson et al., 2011; Mote et al. 2018). Correspondingly, snowpack is one source of potential temperature reconstruction error, as anomalous winter snowpacks relative to mean cool-season temperatures (i.e., high snow in warm years and low snow in cool years) do occur, which can confound the climate response recorded by tree growth (e.g., outlier data points in supporting information Figure S2). However, the relationship of tree growth to snowpack is neither stationary or particularly strong, and attempts at producing reconstructions of snowpack from WBP tree growth did not statistically cross-validate when predictions were compared against removed observed values (data not shown). This suggests the relationships between growth and snowpack were secondary to temperature and tied more closely to the physical temperature-snowpack relationship.

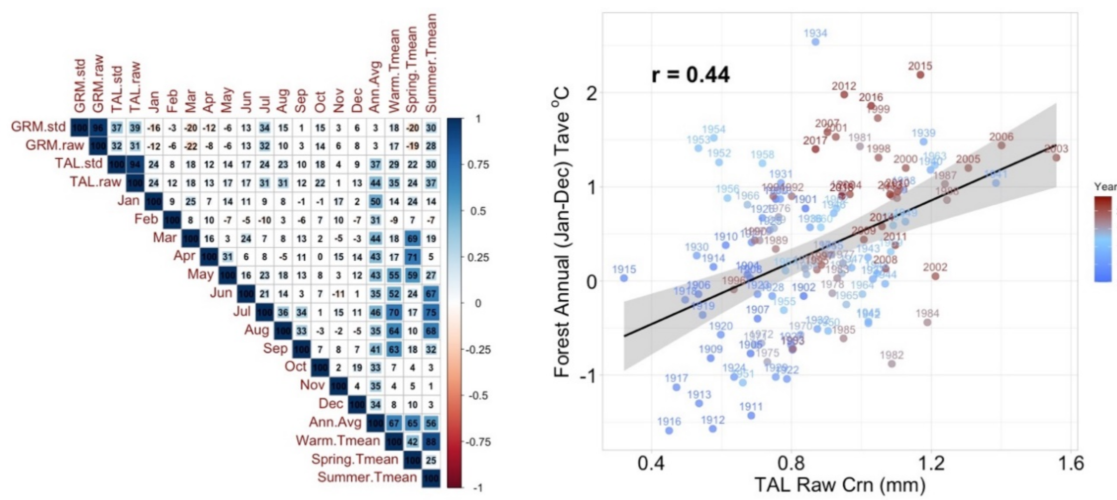

Figure 4. *Left*: Correlation matrix of whitebark pine tree growth (raw mm ring-widths and standardized chronology) for the upper treeline site (TAL) and monthly, seasonal, and annual temperature (°C) from 1900-2018. Only significant relationships ($p < 0.05$) are shown with colored cells. *Right*: Relationship between average annual temperature (°C) and whitebark pine tree- growth (mean annual millimeters; $r = 0.44$; $p < 0.001$). A relatively stable linear relationship between annual temperature and ring-with is shown (black line) and bracketed with 95% confidence intervals (gray shading) that exhibits reduced tree-growth in the early-20th century corresponding to cooler temperatures (blue dots) versus relatively rapid growth rates during more recent decades defined by increasingly warm temperatures (red dots).

3.3 Optimized Temporal Window for Climate Reconstruction

Seasonal partial correlation analyses further indicate that average temperature (°C) is the dominant influence on WBP tree growth at the modern forest site, with the strength of this relationship increasing with increasing length of the seasonal window (from 6 to 22 months) (Figure 5, supporting information Figure S3). In contrast, the potential influence of precipitation as a control on tree growth decreases with increasing season window length comparisons (Figure 5). The long multi-year response of tree growth to temperature is likely due to carbohydrate storage and long needle retention times of these high-elevation conifers (Kipfmueller and Salzer,

2010) and the lagged physiological relationship with climate suggests that the best statistical reconstructions of temperature, in terms of prediction accuracy, occurs with the annual (12-month) and near biennial (22-month) time intervals. However, while the 22-month biennial window exhibits the greatest correlation with tree growth, we opted to also include warm-season (May-Oct) mean temperatures for our analysis. This is because temperatures during the warm season are critical for the survival of living trees at treeline, as well as the formation and persistence of ice at higher elevations. In addition, the strongest correlations between tree growth and temperature occurred during the growing season (Figure 4), suggesting that the growth response is weighted to reflect growing season conditions, even though the strongest statistical relationships are over multi-year windows. The statistically superior 22-month biennial time interval further reflects the importance of growing season temperature on WBP growth, as the 22-month window is centered over two consecutive growing seasons (Figure 5, supporting information Figure S3).

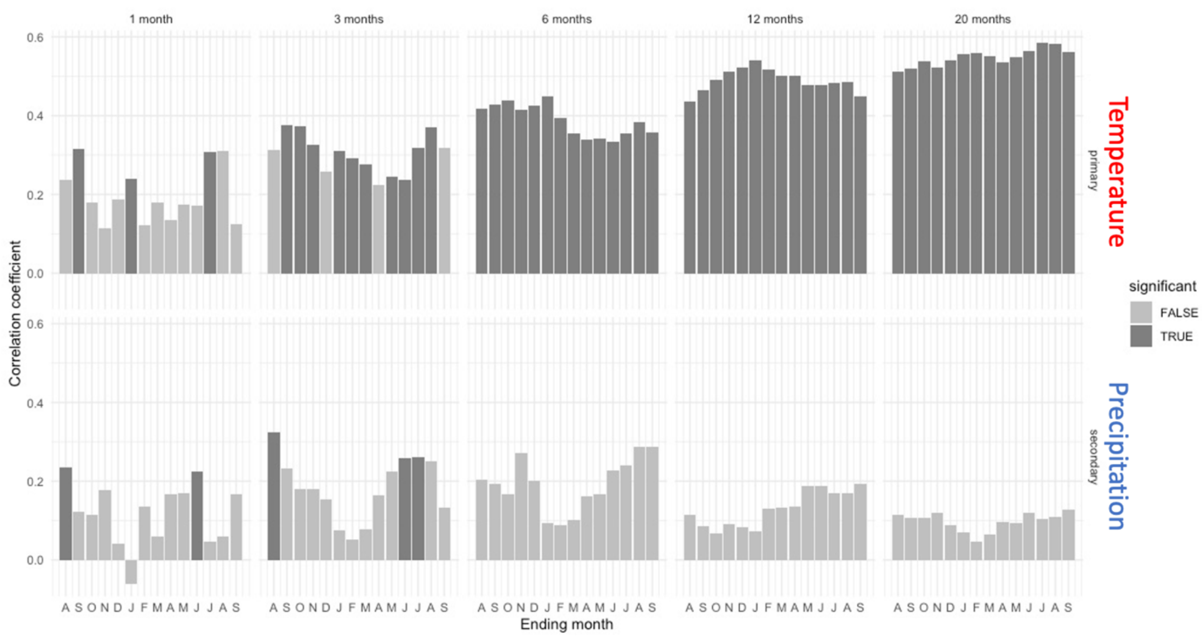

Figure 5. Seasonal partial correlations between temperature (°C), precipitation (mm), and tree growth (raw mm ring-widths) of living whitebark pine trees sampled at the modern treeline forest site.

3.4 Transfer Function Calculation and Calibration-Verification of Climate Reconstructions

To generate prediction-quality statistical relationships between millimeters of average stand-wide growth from the TOL subfossil wood tree-ring chronology to average temperature (°C) at the ice patch site, a transfer function was computed from the stable relationship between tree growth and temperatures observed at the TAL modern forest site over the years 1900-2018. However, radial mean tree growth at the modern forest site was much greater than that of the ice patch subfossil wood chronology. Specifically, the modern forest stand exhibited a minimum average growth rate of 0.32 mm, which was nearly equivalent to the 0.33 mm average stand growth rate estimated for the subfossil wood record (Table 2). This implies that the years of comparable growth in the modern WBP chronology to the subfossil wood are largely associated with the cold temperatures and low growth rate end of each variables distribution (supporting information Figure S1). Since we are making predictions of past temperatures that occur on the colder and slower growth end of the modern distribution, we opted to fit linear and non-linear relationships between average stand-wide tree growth (mm ring-widths) and temperature across the four seasonal windows identified through partial correlation analysis using *MLR* (supporting information Table S1) and *BRNN* (supporting information Table S2, Figure 6). Comparison of the associated cross-validation statistics provided a statistical benchmark to assess if either method produced better (i.e., lower error) predictions of temperature throughout the range and at the extreme ends of the temperature-growth distributions. Furthermore, we were able to use both reconstructions to bracket prediction uncertainty related to the shape (i.e., linear vs. non-linear) of the growth-temperature relationship in our mid-Holocene temperature reconstructions.

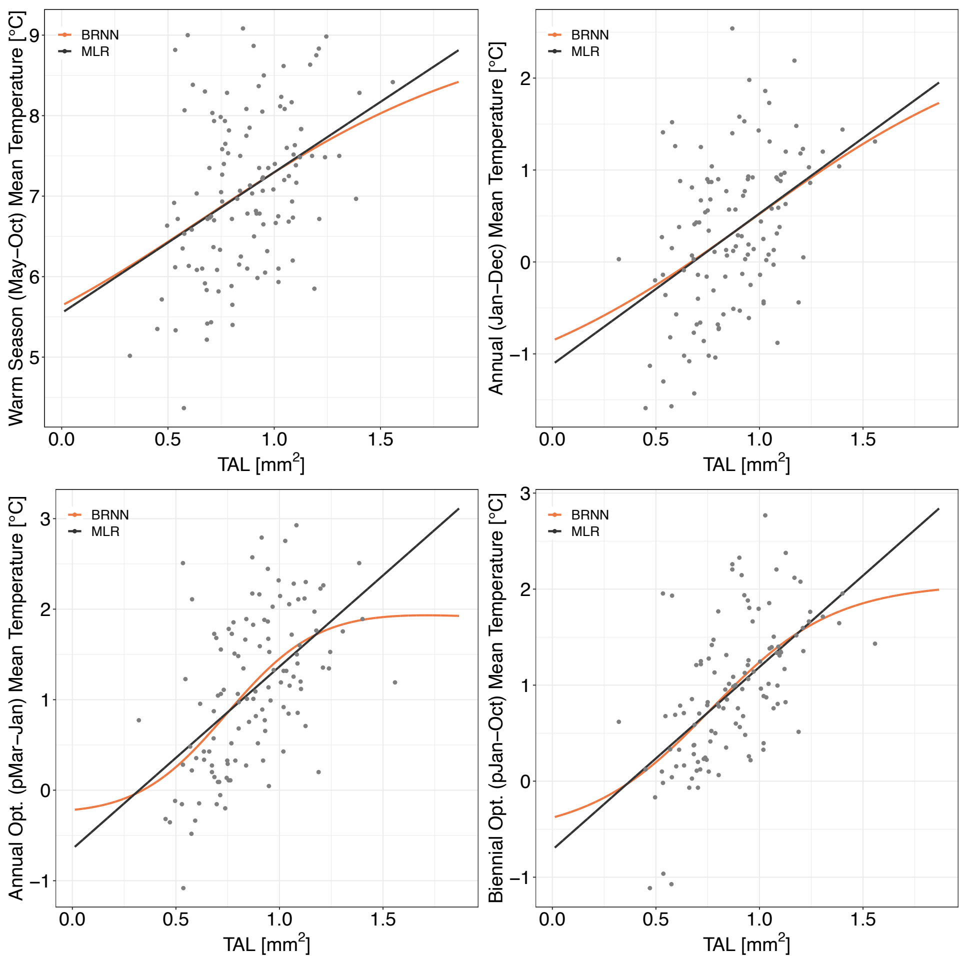

Figure 6. Construction of linear (*top*) and non-linear (*bottom*) transfer functions relating whitebark pine tree growth (mm^2) to temperature (°C) across windows identified through seasonal partial correlation analysis [*top-left*: warm-season (May-October) / *top-right*: annual (January-December) / *bottom-left*: optimized annual (March of the previous year through January of the current year) / *bottom-right*: optimized biennial (January of the previous year through October of the current year).

Over the calibration period (1900-2018) the *MLR* and *BRNN* methods exhibited highly similar results, with the optimized annual and biennial reconstructions producing more accurate predictions overall with smaller associated root mean squared error (Figure 7 and 8). Model performance evaluated using the k-fold cross-validation approach provided a relatively unbiased method for testing model prediction qualities throughout the range of modern temperature observations. For the sign test (*d*) and correlation (*r*) validation metrics, the relative skill in predicting the sign and capturing the variance and trend of the annual temperature departure increases with increased length of the seasonal window, moving from the warm-season (MLR: *d* = 0.507 (validation mean) ± 0.131 (std. dev) / *r* = 0.379 ± 0.284; BRNN: *d* = 0.494 ± 0.124 / *r* = 0.376 ± 0.288) and annual reconstructions to the optimized annual to biennial reconstructions (MLR: *d* = -1.062 ± 0.649 / *r* = -0.762 ± 0.555; BRNN: *d* = -1.091 ± 0.593 / *r* = 0.786 ± 0.509) (Figure 8, supporting information Table S3). The range in standard deviation of the sign test (*d*) and correlation (*r*) validation metrics notably decreases with increased window length (Figure 8, top). In a similar fashion to the coefficient of determination (R^2), the *CE* and *RE* metrics can be interpreted as estimates of shared variance (squared) between the reconstruction predictions and withheld temperature observations, but with the sign of the relationship retained. Thus, predictions with negative *CE* and *RE* values are interpreted as having no prediction skill, with the *CE* statistical test being the more conservative and difficult to pass of the two metrics. When considering the validation *CE* and *RE* metrics, the methods produce nearly equivalent results with *BRNN* slightly, but not significantly, outperforming *MLR* in the optimized seasonal reconstructions (Figure 8, middle). In addition, the mean *CE* and *RE* values shown are positive across all seasonal lengths, suggesting that, on average, each model exhibits prediction skill that increases with season length (up to the biennial reconstruction) even though a subset of the individual 10-fold validation periods fall below zero. Results were similar for *RMSE* and *RRSE*, with annual prediction error declining for both calibration and prediction subsets, moving from the warm-season reconstruction (MLR: *RMSE* = 0.902 ± 0.176 / *RRSE* = 0.982 ± 0.152; BRNN: *RMSE* = 0.904 ± 0.175 / *RRSE* = 0.984 ± 0.147) to the optimized annual and biennial seasonal reconstructions (MLR: *RMSE* = -0.862 ± 0.586 / *RRSE* = -0.962 ± 0.617; BRNN: *RMSE* = -0.887 ± 0.537 / *RRSE* = -0.989 ± 0.565) (Figure 8, bottom, supporting information Table S3).

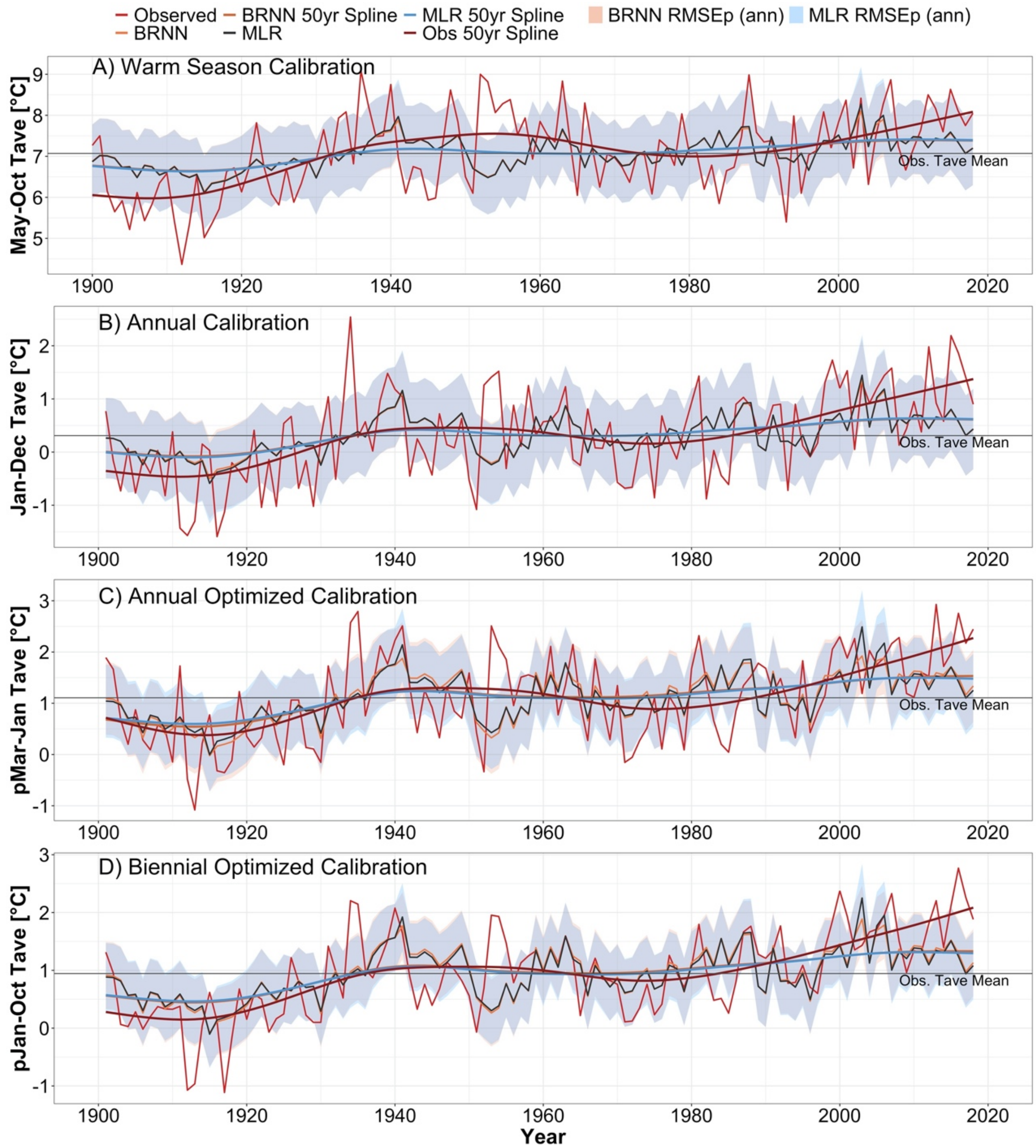

Figure 7. Temperature (°C) reconstructions (from 1900-2018) derived from live whitebark pine stand average tree growth chronology (TAL raw) at the upper treeline forest site. Seasonal reconstructions were developed using two methods: least-squares linear regression (*MLR*; light blue) and artificial neural networks with the Bayesian regularization training algorithm (*BRNN*; orange) and include (A) warm-season [May-October], (B) annual [January-December], (C) annual optimized [previous March-current January], and (D) biennial optimized [previous January-current October]. The time series data were fit with a 50-year spline (smooth line) with 95% confidence intervals (gray shading).

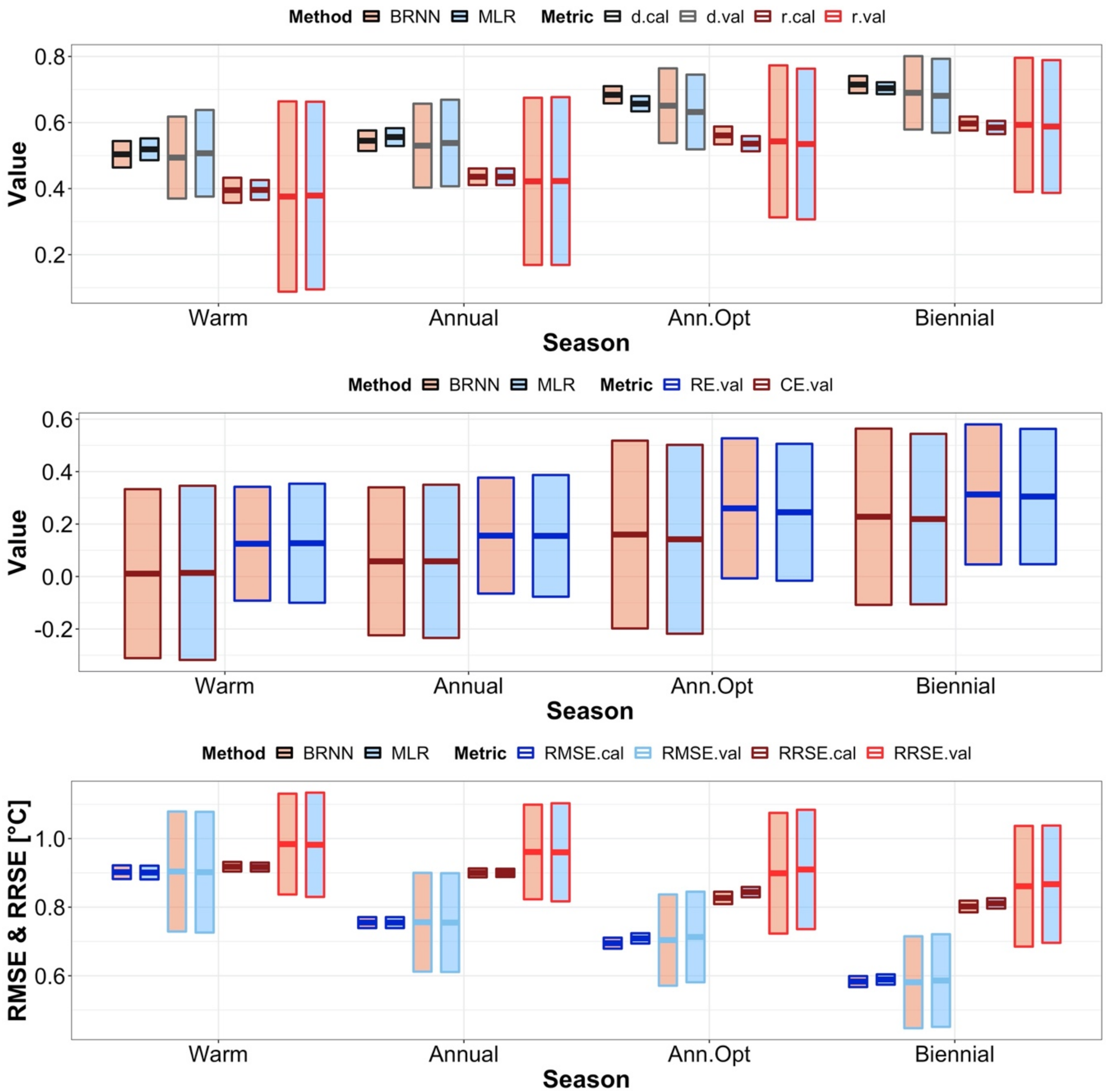

Figure 8. Plots of the (*top*) mean correlation (*r*) and sign test (*d*) values, (*middle*) mean reduction of error (*RE*), and coefficient of efficiency (*CE*), and (*bottom*) root mean squared error (*RMSE*) and root relative squared error (*RRSE*) values (all values bounded by ± 1 s.d.) for the calibration (.cal) and verification (.val) data subsets produced by the bootstrapped 10-fold cross-validation method employed in the two reconstruction methods: least-squares linear regression (*MLR*; light blue) and artificial neural networks with the Bayesian regularization training algorithm (*BRNN*; orange).

In addition to k-folds cross-validation, we also evaluated performance of the *MLR* and *BRNN* methods using the central-edge test, whereby a subset of the extreme (edge) data points are estimated as validation data (Jevšenak et al., 2018). For this analysis, the sign test (*d*) and correlation (*r*) results suggest that both the *BRNN* and *MLR* methods predict extreme warm and cold conditions well, with the *MLR* method performing slightly, though not significantly better in most cases (Figure 9, supporting information Table S4). The seasons with the best prediction performance are the (non-optimized) annual (MLR: d = 0.901 / r = 0.856; BRNN: d = 0.883 / r = 0.859) and biennial optimized reconstructions followed by the annual optimized then warm-season reconstructions (MLR: d = 0.761 / r = 0.655; BRNN: d = 0.735/ r = 0.66). However, the reduced spread between central calibration and edge validation statistics for the annual optimized and biennial optimized reconstructions suggests that these are superior models, although all models perform reasonably well in predicting values at the extremes of the distribution (Figure 9, supporting information Table S4).

In terms of *CE* and *RE*, the methods produced nearly equivalent results though the *BRNN* method outperforms *MLR* in predicting the extreme values for the optimized annual (MLR: *CE* = 0.164 / *RE* = 0.168; BRNN: *CE* = 0.381 / *RE* = 0.384) and optimized biennial reconstructions (MLR: *CE* = 0.431 / *RE* = 0.432; BRNN *CE* = 0.529 / *RE* = 0.529). Root-mean-square error and *RRSE* is greatly reduced for predicted values in the annual reconstruction (MLR: *RMSE* = 0.499 / *RRSE* = 0.53; BRNN: *RMSE* = 0.518 / *RRSE* = 0.55), followed by the biennial optimized reconstruction, with mixed results shown for the optimized warm-season and optimized annual reconstruction (MLR: *RMSE* = 0.934 / *RRSE* = 0.914; BRNN: *RMSE* = 0.804 / *RRSE* = 0.787) (Figure 9, supporting information Table S4). This analysis indicates that the biennial optimized reconstruction performs best in terms of prediction accuracy throughout the range of values, but the annual reconstruction excels with prediction accuracy at the extremes (Figure 9). Though it should be noted this result may arise solely by chance.

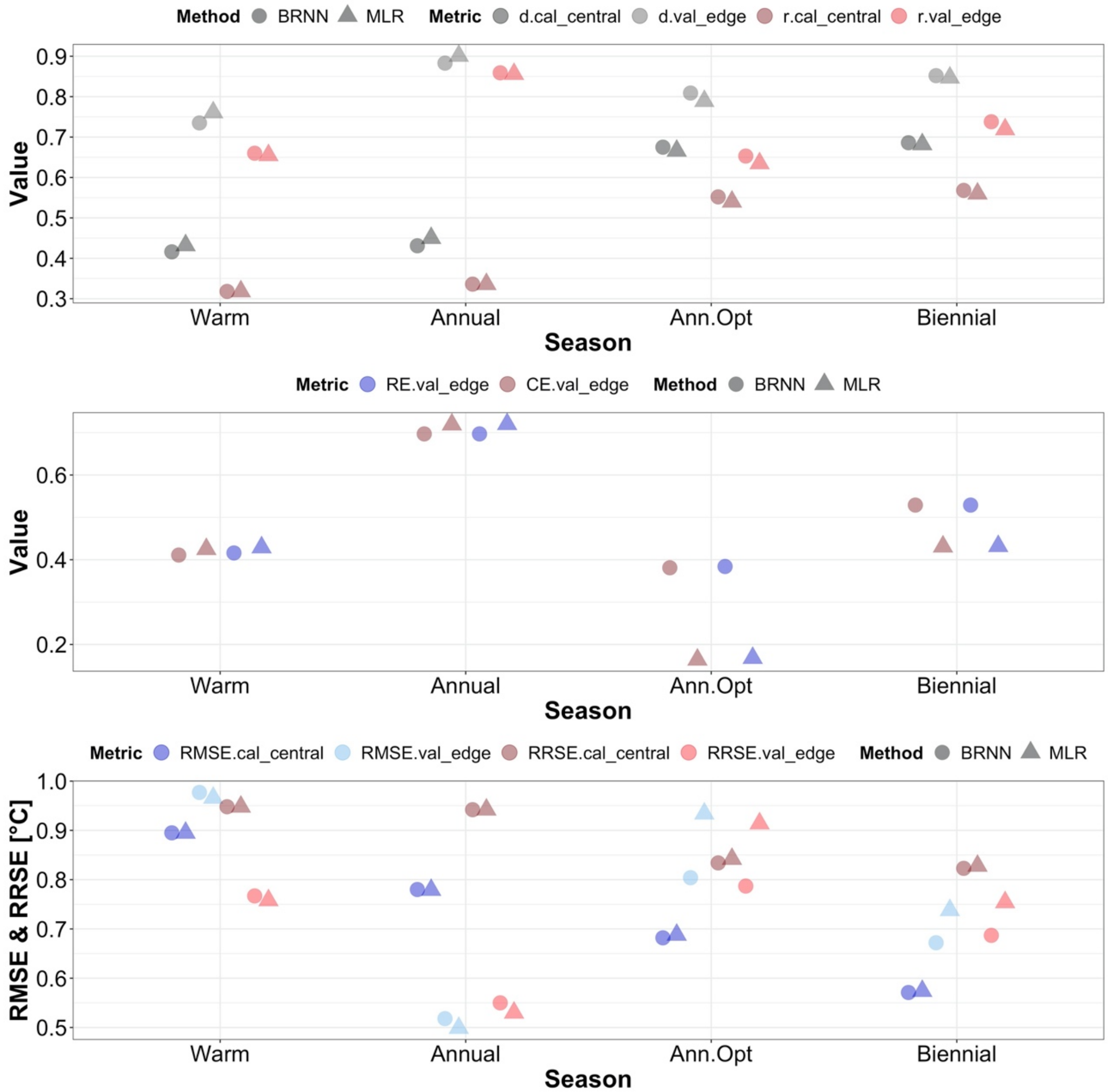

Figure 9. Plots of the (*top*) mean correlation (*r)* and sign test (*d)* values, (*middle*) mean reduction of error (RE), and coefficient of efficiency (*CE*), and (*bottom*) root mean squared error (*RMSE*) and root relative squared error (*RRSE*) values produced by the central-edge test for the central calibration (.cal_central) and edge verification (.val_edge) data subsets run on the two reconstruction methods: least-squares linear regression (*MLR*; triangles) and artificial neural networks with the Bayesian regularization training algorithm (*BRNN*; circles). *Note*: The spread between the central calibration and the edge validation values for the warm-season and annual indicates the models do particularly well predicting temperature values on extremely warm or cold years.

3.6 Mid-Holocene Temperature Reconstruction

The linear (*MLR*) and non-linear (*BRNN*) transfer functions developed and tested above, were then applied to the subfossil WBP raw average growth chronology (TOL) to reconstruct mid-Holocene, warm-season to biennial average temperatures over four centuries covering a period of 5,900-5,436 (± 51.3) years BP (supporting information Figure S4). Due to the effects of regression, reduced distribution of the subfossil WBP chronology (supporting information

Figure S1), combined with extrapolation of regression predictions beyond the cold, low-growth end of the modern growth-temperature distribution, interannual variance in the temperature estimates of each reconstruction is highly compressed (supporting information Figure S4). However, when bounded by the prediction *RMSE* and averaged over climatologically relevant time frames (e.g., 30-50 years), we argue the mean and range of the reconstructed temperature estimates represent the long-term seasonal temperature mean with the RMSE bounding box representing the range of interannual variability. This relationship is shown in Figure 7, where annual predictions closely track the long-term observed temperature mean and trend (see the observed and reconstructed 50-year splines), and the *RMSE* of the reconstruction overlaps the range of observed temperature values. With this climatological interpretation in mind, we present our modern and mid-Holocene average temperature reconstruction time series as 50-year binned box and violin plots bounded by the *RMSE* of the prediction, with a focus on the warm-season and optimized biennial reconstructions (Figure 10). We feature these two seasonal temperature reconstructions due to the prediction quality of the biennial model and their role in governing treeline, snow and ice dynamics. See supporting information Figure S5 for the optimized and non-optimized annual reconstructions.

The warm-season and biennial average temperature reconstructions show similar centennial-scale variability over the mid-Holocene period (Figure 10). Over the first half of the reconstruction (5,900-5,650 years BP), temperatures varied around average warm-season (biennial) means of 6.19°C (-0.03 °C) for both the linear (MLR) and non-linear (BRNN) versions of the reconstruction. A sustained ~200-year temperature decline initiated around 5,650 years BP continued through the remainder of the reconstruction, ending at 5,436 years BP (Figure 10). Over the last part of the reconstruction (5,450-5,436 years BP), mean warm-season and biennial average temperatures for the BRNN (MLR) models declined to 5.80 °C (5.74 °C) and -0.30 °C (-0.50 °C) respectively. Taken together, a mean temperature change of -0.42 °C (warm-season) and -0.37 °C (biennial) is estimated to have occurred between the early half of the record (5,900-5,650 years BP) and the cold end period of the record (5,450-5,436 years BP).

Both the warm-season and biennial reconstructions show average mid-Holocene annual temperatures descending to early-20th century median ice patch temperature levels (Figure 10). Observed and reconstructed temperature estimates over the 20th and early 21st century (1900-2018) are plotted alongside the mid-Holocene reconstructions for both the warm-season and biennial seasonal intervals (Figure 10, right). Early-to-mid-20th century temperature estimates are within the predicted range of mid-Holocene ice patch temperature estimates, while recent time periods trend toward increasingly warmer temperatures, an opposing trend compared to estimated mean temperatures over the last two centuries of the mid-Holocene reconstructions (Figure 10). Over recent decades (2001-2020), the distribution of annual average temperatures has extended outside the lower 25% quartile of observed annual warm-season and biennial average temperatures at the ice patch site, rapidly approaching the annual average temperatures of the forest site.

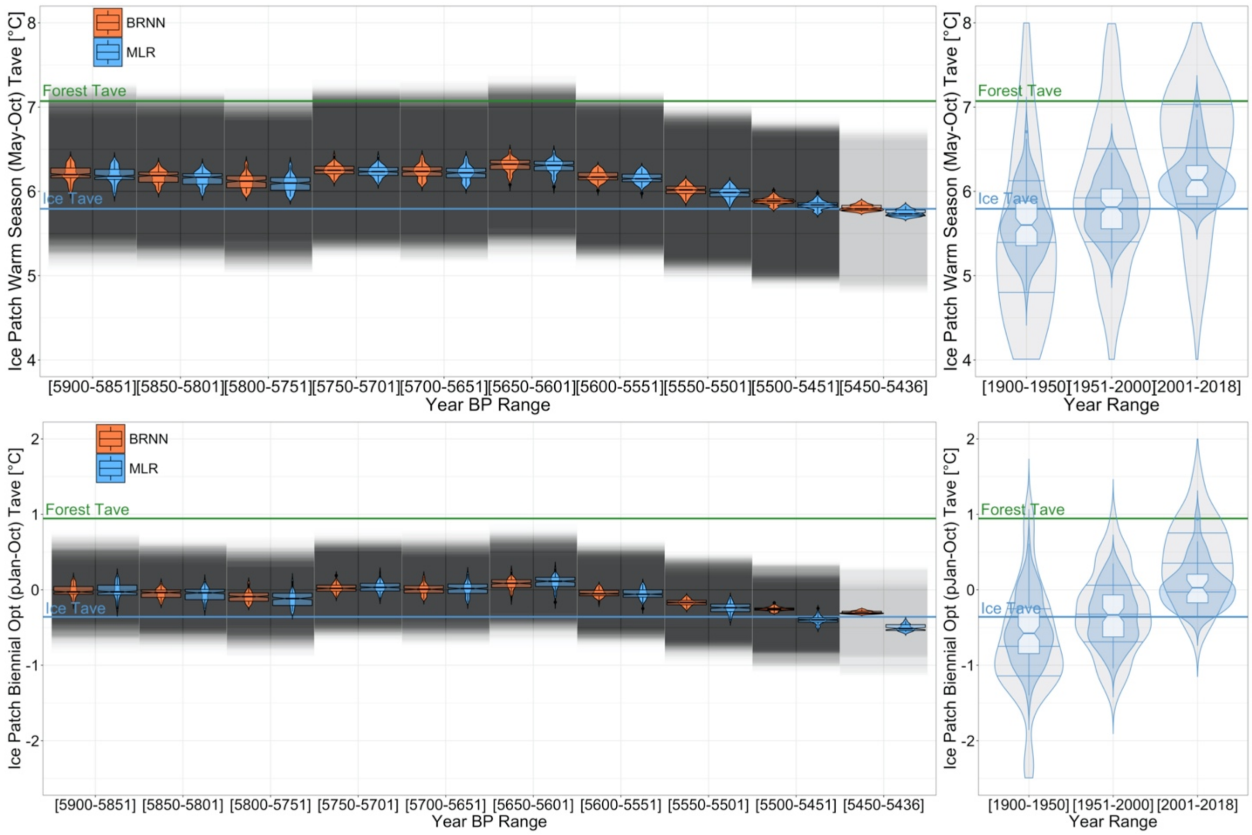

Figure 10. *Left*: 50-year bins of mid-Holocene mean temperature estimates (5,900-5,436 years BP) at the ice patch site derived using the MLR (light blue) and BRNN (orange) methods and bounded by the RMSE of the prediction (gray boxes) for the warm-season (May-Oct) reconstruction (*top*) and for the optimized biennial reconstruction (*bottom*). *Right*: 50-year distribution of annual average temperatures (1900-2018) from the instrumental record (light gray violin plots with horizontal lines plotted showing the median (50%) and 25% to 75% interquartile range) and temperature estimates from the reconstructions (blue violin plots).

4. DISCUSSION

In this study, we present the first crossdated and statistically robust mid-Holocene tree-ring chronology and subsequent novel climate reconstruction developed from subfossil wood preserved by an ice patch from the NRM region. Radiocarbon dating revealed that the subfossil WBP tree boles emerging from the margins of the Tolman ice patch grew between 5,947 to 5,436 years BP (± 51.3 years) and are remnants of a WBP forest that established over 120 m above present day treeline at the end of the mid-Holocene warm period.

High-elevation WBP stands can be limited in growth by a range of climatic variables (i.e., temperature, snowpack accumulation, total precipitation) across a range of seasonal intervals (i.e., current year growing season and annual conditions to multi-year climatic conditions). To investigate growth-climate relationships relevant to the subfossil ice patch wood, we developed a modern tree-ring chronology from the nearest upper treeline WBP forest and identified temperature to be the major climatic variable limiting modern tree growth at the adjacent forest site (Figure 4). To a lesser extent, snowpack represented a secondary growth limitation and likely one of the primary sources of reconstructed temperature error (supporting information Figure S2).

The stable relationship between interpolated temperature observations and stand-average WBP tree growth at the adjacent forest site allowed for the use of linear and non-linear transfer functions to successfully reconstruct temperature (°C) from tree-ring measurements of stand-average growth (mm). In terms of prediction quality, these temperature-growth relationships are statically robust, passing rigorous k-folds and central-edge cross-validation tests, for the warm-season and improve with increasing seasonal length out to a near biennial 22-month period during and preceding the current year of growth (Figures 7 to 9). The subfossil WBP record exhibited a lower mean and range of stand-wide growth in comparison to the modern WBP chronology (Table 2, supporting information Figure S1), and these growth rate characteristics, along with the dominant low-frequency (i.e., 32-128 year multidecadal to centennial-scale) variability of the record, further support the notion that temperature governs stand-wide growth, more so than precipitation, drought, or snowpack (Figures 4, 5, supporting information Figures S2, S6). Conversely, moisture limited sites tend to exhibit greater power at much higher frequencies (i.e., 2-20 year interannual- to decadal-scale) in response to the common interannual drought or precipitation variability across the West. These results support the use of modern WBP temperature-growth relationships to be applied in the form of robust transfer functions to the subfossil growth chronology to generate multi-century estimates of temperature variability in this region of the NRM during the mid-Holocene.

The linear (*MLR*) and non-linear (*BRNN*) transfer function models produce a slightly different range of prediction estimates throughout both the warm-season and biennial reconstructions. The difference between the two models is most noticeable over the coldest 100-114 year period from 5,550-5,436 years BP (warm-season BRNN = 5.93 °C; MLR = 5.89 °C / biennial optimized BRNN = -0.27 °C; MLR = -0.42 °C). This is because the models calculate slightly different predictions at the extreme ends of the estimated temperature distributions, where the *MLR* model fits a rigid linear regression, predicting a slightly colder estimated temperature range in the last 100 years of the reconstructed time period than the non-linear *BRNN* model. Although some differences in estimated temperature exist, the common low-frequency variation and overall trend in temperature is replicated by both models (Figure 10).

The warm-season and biennial average temperature reconstructions show centennial-scale variability over the first 250-300 years of the reconstructed period (Figure 10, supporting information S6). During the mid-Holocene time period, average temperatures fluctuated by a quarter to a third of a degree (°C) within a temperature range that was conducive but suboptimal for WBP tree growth. A period of sustained cooling initiated around ~5,650 years BP and mid-Holocene annual temperatures gradually decreased for the remainder of the reconstruction, eventually reaching temperature levels similar to those observed in the early 20th century (e.g., 5.87 °C [BRNN] / 5.82 °C [MLR] for the warm-season reconstructions and -0.27 °C [BRNN] / -0.42 °C [MLR] for the biennial reconstructions). Importantly, we note a mean warm-season (biennial) temperature change of -0.44 °C (-0.38 °C) that occurred over the course of our reconstruction (5,900-5,436 years BP) that coincides with stand-wide growth rate declines and eventual death of the trees that once grew where the Tolman ice patch now resides. This reconstructed regional cooling of -0.44 °C (-0.38 °C) over a 464-year period had significant ecological consequences, as it resulted in reduced treeline elevations and enabled snow and ice to persist through growing season warmth in certain high-elevation areas predisposed to ice accumulation across the Beartooth Plateau. Eventually, mid-Holocene temperatures decreased past a threshold of growing season mean temperatures required for photosynthesis, carbon accumulation, and tree survival (Bunn et al 2018; Körner, 1998; Körner & Paulsen, 2004). Based on our reconstructions, we identified these warm-season (biennial) median average temperature threshold values as 5.82 °C [MLR] to 5.87 °C [BRNN] (-0.42 °C [MLR] to -0.27 °C [BRNN]), though bounded by broad uncertainties (Figure 10).

Potential climate forcings underlying the estimated mid-Holocene temperature declines exhibited in our reconstructions may be elucidated through comparisons with high-resolution, global transient climate models. For mid- to high-latitude regions from 30 °N, poleward, Bader et al. (2020) simulated gradual mid-Holocene cooling trends in annual average temperatures that accelerate around 4,000 years BP. Most relevant to our mid-Holocene temperature reconstructions, the authors show a strong region of cooling centered over the western U.S., driven by increasing Arctic summer sea-ice concentration and decreasing summer high-latitude solar radiation [see Figures 2 and 3 in Bader et al. (2020)]. In addition to the general cooling trend, Bader et al. (2020) speculate that a severe Northern Hemisphere high-latitude cooling anomaly centered around ~5,200 years BP [see Figure S2 in Bader et al. (2020)], may have been forced by multiple centuries of increased high latitude vulcanism, based largely on the Greenland Ice Sheet Project (GISP 2) sulfate record. Conversely, the sulfate record from the GISP2 ice core may have originated from biogenic sources. If there was broad high-latitude vulcanism at this time, the rapid cooling event identified in the Bader et al. (2020) transient climate simulation aligns well with the death of the WBP trees at the Tolman ice patch on the Beartooth Plateau of northwestern Wyoming.

A rapid cooling event related to large-scale volcanic processes would help explain the high degree of WBP tree bole preservation (e.g., the lack of severe weathering of the outer sapwood), which suggests that sustained ice cover could have taken as little as several decades to establish and entomb the ancient forest. As summer solar insolation decreased, growing seasons became progressively shorter and cooler, eventually surpassing a warm-season (biennial) temperature threshold of ~5.8 °C (-0.34 °C) where tree growth was no longer possible (Bunn et al 2018; Körner & Paulsen, 2004). This regional cooling is further corroborated by limnological studies that show an onset of cooler summers (and/or extended winter season conditions) that lead to increased lake levels after 5,600 years BP (Shuman et al., 2017), followed by a decline in carbonate-rich sediments around 5,000 years BP, which is indicative of summer season cooling (Whitlock et al., 2012). This disparity in temperature on the Beartooth Plateau between modern times and those of the mid-Holocene is evident in a simple comparison of measured growth rates of the subfossil wood relative to the modern WBP trees growing at upper treeline (Table 2, supporting information Figure S1).

It is possible that temperature-related physiological stress from these increasingly cooler conditions limited the amount of carbon fixation required to maintain respiration and the subfossil WBP trees struggled to build sufficient carbohydrate reservoirs, eventually leading to carbon starvation and death (Smith et al., 2003) although we do not have data to test this hypothesis. Interestingly, the subfossil WBP trees do not exhibit the physiological features of a typical treeline stand (e.g., sparsely distributed krummholz form trees), indicating that treeline would have been even higher in elevation than where the ice patch sits today (above 3,091 m).

The subfossil WBP trees grew at a time when summer temperatures were warm enough to sustain full-form tree growth (e.g., >25 cm DBH) at these high elevations. During our field surveys, we did not identify suspended root collars or stunted krummholz growth forms melting out of the ice patch, suggesting that the subfossil WBP forest stand originated from a mature legacy of subalpine WBP regeneration that would have established over the course of several thousands of years during the preceding mid-Holocene thermal maximum.

It is also possible that a wind event could have contributed to mortality of the ancient forest, or simply knocked the subfossil tree stems over after they had already died. For instance, we did find upturned root bowls and shattered trunks with the main stems all suggesting an easterly high wind event(s) could have impacted the stand. However, there isn't clear synchrony across outer ring dates of the subfossil wood, negating the possibility that one single event (e.g., wind, avalanche, human-use) could have been responsible for widescale tree mortality across the stand. It's also unlikely that ice flow or snow avalanche killed or sheared the trees as their trunks and upturned roots would have been oriented in the opposite direction than they were found with death dates again aligning in time. In addition, low slope angles (<10 degrees) at the ice patch site are not conducive for snow avalanches or ice flow. We also did not find evidence of widescale insect-related mortality in the subfossil wood, with only one *J*-shaped gallery being found among the 34 surveyed stems and little direct evidence for beetle kill or damage in the preserved cambium (e.g., blue-staining in the outer wood from beetle-associated fungal symbionts).

Based on the relationship of modern tree growth to the ancient WBP forest (Table 2, supporting information Figure S1), it is evident that exceptional warming over the past half-century has increased productivity in treeline forests of the Beartooth Plateau, and in other high-elevation forests throughout the western U.S. more broadly (Salzer et al., 2009; Paulsen and Korner 2012). Whitebark pine trees at the modern forest site exhibit strong, positive relationships with temperature, which has increased over recent decades (Figures 7, 10), and the temperature-tree growth threshold is now migrating up slope to higher altitudes. Based on our mid-Holocene reconstructions, we found average warm-season (biennial) temperature values of 6.13 °C (-0.08 °C) for the period of 5,900-5,436 years BP, compared to 6.42°C (0.37°C) for the period of 2001-2020, which indicates that conditions over the first two decades of the 21st century were approximately 0.29 °C (0.45 °C) warmer than the 464-year span of our mid-Holocene reconstruction. In addition, from the period of 1950-2020 warm-season (biennial) average temperatures have further increased by 0.72 °C (0.59 °C), relative to 1900-1950, and in the most recent decades (2001-2020), the distribution of temperatures at the ice patch location have extended beyond the lower quartile (25%) of observed average temperatures, rapidly approaching the annual average temperatures of the upper treeline forest site (Figure 10, right). This 21st century regional warming corresponds with the net negative mass balance of the ice patch and exposure of the preserved subfossil logs and suggests that the ice patch will fully ablate and conditions at the site will once again become suitable for tree establishment, likely within as little as a few decades.

5. CONCLUSIONS

The discovery of the ancient stand of mature WBP trees entombed in ice over 120 m above present day treeline provides a unique opportunity to reconstruct mid-Holocene climatic conditions that led to dramatic ecosystem change in this dynamic high-elevation environment. Our reconstruction is one of the first floating chronologies of subfossil wood recovered from a melting ice patch in the NRM and reveals mid-Holocene warm-season (biennial) temperatures declined past a critical threshold of 5.8 °C (-0.34 °C), whereby ice persisted and accumulated across the landscape, eventually burying and preserving the ancient forest in an ice patch that persisted from 5,000 years BP to present day.

It is difficult to assess how anthropogenic warming will influence the future habitability of WBP across the full range of its distribution. Climate-related shifts in environments suitable for tree growth and seedling establishment, potential disruption in the caching behavior of the species primary seed distributer Clarks nutcrack (*Nucifraga columbiana*), and complex disturbance synergies may leave the species vulnerable to elevated mortality across much of its contemporary range. However, we observed a positive response of modern WBP trees to increases in 20th and 21st century temperatures and our results suggest that conditions at the current ice patch location will likely, within decades, once again become favorable for treeline establishment.

The Tolman ice patch subfossil WBP chronology provides a unique dataset recording stand-wide tree decline and mortality coinciding with regional cooling and ice patch formation. Our findings highlight the dynamic nature of both high alpine climate and the ecological response of vegetation to these shifting abiotic processes. Results also provide important information on the future trajectory of high-elevation ice patches in the GYE more broadly. While the ice patches of the Beartooth Plateau have persisted for thousands of years, the stress of recent warming is unprecedented and has accelerated the disappearance of ice patches in the region, a loss of valuable archeological and paleoenvironmental resources (Chellman et al., 2021; Lee and Puseman, 2017). This high-quality paleo-ecological dataset reveals a major shift in the alpine and forest ecotone on the Beartooth Plateau following the mid-Holocene warm period and offers further insight on the thermal limits of WBP trees. This record also provides new insights into the climatic conditions favorable for ice patch development and persistence in the Greater Yellowstone Ecosystem.

CONCLUSION

This study contributes add a high-quality, chronologically constrained temperature reconstruction from the mid-Holocene and provides estimated temperatures values limiting the elevational distribution of WBP trees on the Beartooth Plateau. Temperature changes in ancient times are of comparative value to the study of modern temperature change. This subfossil tree-ring growth records variability in mean temperatures on varying seasonal lengths and refines the temporal interpretation of other paleo-climate proxy records further elucidating the regional effects of hemispheric climate variability recorded by global temperature reconstructions. Using this subfossil WBP chronology to inform more temporally coarse records will strengthen the projections of paleo-proxy based Earth system models, which are used to predict future changes in climate and ecosystem response to warming. Whitebark pine forests across the western U.S. are experiencing extensive mortality and broad ecosystem changes that threaten regeneration. Better understanding the capacity for these ecosystems to respond and adapt to major climatic regime shifts is a critical for ecosystem management.

REFERENCES CITED

Abatzoglou, J. T., Dobrowski, S. Z., Parks, S. A., & Hegewisch, K. C. (2018). TerraClimate, a high-resolution global dataset of monthly climate and Climatic Water Balance from 1958–2015. *Scientific Data*, *5*(1). https://doi.org/10.1038/sdata.2017.191

Bader, J., Jungclaus, J., Krivova, N., Lorenz, S., Maycock, A., Raddatz, T., Schmidt, H., Toohey, M., Wu, C.-J., & Claussen, M. (2020). Global temperature modes shed light on the holocene temperature conundrum. *Nature Communications*, *11*(1). https://doi.org/10.1038/s41467-020-18478-6

Barnett, T. P., Pierce, D. W., Hidalgo, H. G., Bonfils, C., Santer, B. D., Das, T., Bala, G., Wood, A. W., Nozawa, T., Mirin, A. A., Cayan, D. R., & Dettinger, M. D. (2008). Human-induced changes in the hydrology of the Western United States. *Science*, *319*(5866), 1080–1083. https://doi.org/10.1126/science.1152538

Benedict, J. B., Benedict, R. J., Lee, C. M., & Staley, D. M. (2008). Spruce trees from a melting ice patch: Evidence for holocene climatic change in the Colorado Rocky Mountains, USA. *The Holocene*, *18*(7), 1067–1076. https://doi.org/10.1177/0959683608095578

Brown, P. M., (1996) OLDLIST: a database of maximum tree ages. Tree Rings, Environment, and Humanity: Proc. of the Int. Conf., Arizona (Tucson). 17-21 May, 1994 *Radiocarbon* vol 1996, pp 727-31

Chellman, N., McConnell, J. R., Arienzo, M., Pederson, G. T., Aarons, S. M., & Csank, A. (2017). Reassessment of the upper fremont glacier ice-core chronologies by synchronizing of ice-core-water isotopes to a nearby tree-ring chronology. *Environmental Science & Technology*, *51*(8), 4230–4238. https://doi.org/10.1021/acs.est.6b06574

Chellman, N. J., Pederson, G. T., Lee, C. M., McWethy, D. B., Puseman, K., Stone, J. R., Brown, S. R., & McConnell, J. R. (2021). High elevation ice patch documents holocene climate variability in the northern Rocky Mountains. *Quaternary Science Advances*, *3*, 100021. https://doi.org/10.1016/j.qsa.2020.100021

Cook, E.R. 1985. A time series approach to tree-ring standardization. PhD dissertation, University of Arizona Press, Tucson, 171 pp

Cook, E. R., & Peters, K. (1997). Calculating unbiased tree-ring indices for the study of climatic and environmental change. *The Holocene*, *7*(3), 361–370. https://doi.org/10.1177/095968369700700314

Cook, E.R., P.J. Krusic, R.H. Holmes, and K. Peters. (2007). Program ARSTAN, version 41d. www.ldeo.columbia.edu/tree-ring- laboratory

Coulthard, B. L., Anchukaitis, K. J., Pederson, G. T., Cook, E., Littell, J., & Smith, D. J. (2021). Snowpack signals in North American tree rings. *Environmental Research Letters*, *16*(3), 034037. https://doi.org/10.1088/1748-9326/abd5de

Daly, C., M. Halbleib, J. I. Smith, W. P. Gibson, M. K. Doggett, G. H. Taylor, J. Curtis, & P. P. Pasteris. (2008). Physiographically Sensitive Mapping of Climatological Temperature and Precipitation across the Conterminous United States. *International Journal of Climatology* 28, 2031-2064

Dixon, E. J., Callanan, M. E., Hafner, A., & Hare, P. G. (2014). The emergence of glacial archaeology. *Journal of Glacial Archaeology*, *1*, 1–9. https://doi.org/10.1558/jga.v1i1.1

Douglas, A.E., (1941). Crossdating in Dendrochronology, *Journal of Forestry*, 39(10), 825–831, https://doi.org/10.1093/jof/39.10.825

Fritts, H. C. (1976). Tree Rings and Climate. Academic Press, New York, N.Y.

Foresee, F. D., & Hagan, M. T. (1997). Gauss-Newton approximation to Bayesian learning. *Proceedings of International Conference on Neural Networks (ICNN'97)*. https://doi.org/10.1109/icnn.1997.614194

Gavin, D. G., Henderson, A. C. G., Westover, K. S., Fritz, S. C., Walker, I. R., Leng, M. J., & Hu, F. S. (2011). Abrupt holocene climate change and potential response to solar forcing in Western Canada. *Quaternary Science Reviews*, *30*(9-10), 1243-1255. https://doi.org/10.1016/j.quascirev.2011.03.003

Glen, J.W. The creep of polycrystalline ice. (1955). *Proceedings of the Royal Society of London. Series A. Mathematical and Physical Sciences*, *228*(1175), 519-538. https://doi.org/10.1098/rspa.1955.0066

Grudd, H., Briffa, K. R., Karlén, W., Bartholin, T. S., Jones, P. D., & Kromer, B. (2002). A 7400-year tree-ring chronology in northern Swedish Lapland: Natural climatic variability expressed on annual to Millennial Timescales. *The Holocene*, *12*(6), 657–665. https://doi.org/10.1191/0959683602hl578rp

Hare, P. G., Thomas, C. D., Topper, T. N., & Gotthardt, R. M. (2012). The Archaeology of Yukon Ice Patches: New Artifacts, observations, and insights. *ARCTIC*, *65*(5). https://doi.org/10.14430/arctic4188

Haslett, J., & Parnell, A. (2008). A simple monotone process with application to radiocarbon-dated depth chronologies. *Journal of the Royal Statistical Society: Series C (Applied Statistics)*, *57*(4), 399–418. https://doi.org/10.1111/j.1467-9876.2008.00623.x

Hoadley, R. B. (1990). Identifying wood accurate results with simple tools. The Taunton Press, Newtown, U.S.A. *IAWA Journal*, *12*(1), 84. https://doi.org/10.1163/22941932-90001207

Holmes, R.L. (1983). Computer-assisted quality control in tree-ring dating and measurement. *Tree Ring Bulletin 44*, 69-78.

Jevšenak, J., Levanič, T.; Džeroski, S. (2018). Comparison of an optimal regression method for climate reconstruction with the compare_methods() function from the dendroTools R Package. *Dendrochronologia, 52*, 96-104. https://doi.org/10.1016/j.dendro.2018.10.001

Jevšenak, J., Levanič, T., 2018. dendroTools: r package for studying linear and nonlinear responses between tree-rings and daily environmental data. *Dendrochronologia 48*, 32-39.

Kellogg, R. M., Rowe, S., Koeppen, R. C., & Miller, R. B. (1982). Identification of the wood of the soft pines of western North America. *IAWA Journal*, *3*(2), 95–101. https://doi.org/10.1163/22941932-90000757

Kipfmueller, K. F., & Salzer, M. W. (2010). Linear Trend and climate response of five-needle pines in the western United States related to treeline proximity. *Canadian Journal of Forest Research*, *40*(1), 134–142. https://doi.org/10.1139/x09-187

Körner, C. (1998). A re-assessment of high elevation treeline positions and their explanation. *Oecologia, 115*(4), 445-459. https://doi.org/10.1007/s004420050540

Lee, C.M., (2010). Global warming reveals wooden artefact frozen over 10,000 years ago in the Rocky Mountains. *Antiquity,84*(325).

Lee, C. M., & Puseman, K. (2017). Ice patch hunting in the Greater Yellowstone area, Rocky Mountains, USA: Wood shafts, chipped stone projectile points, and bighorn sheep (ovis canadensis). *American Antiquity*, *82*(2), 223–243. https://doi.org/10.1017/aaq.2016.32

Lee, C.M., (2018). Final Report - Continuing archaeological and paleobiological reconnaissance of perennial ice and snow patches, Custer Gallatin National Forest, Montana and Shoshone National Forest. INSTAAR, Wyoming.

Licciardi, J. M., & Pierce, K. L. (2008). Cosmogenic Exposure-age chronologies of Pinedale and Bull Lake glaciations in Greater Yellowstone and the Teton Range, USA. *Quaternary Science Reviews*, *27*(7-8), 814–831. https://doi.org/10.1016/j.quascirev.2007.12.005

MacKay, D. J. (1992). Bayesian interpolation. *Neural Computation, 4*(3), 415–447. https://doi.org/10.1162/neco.1992.4.3.415

Marcott, S. A., Shakun, J. D., Clark, P. U., & Mix, A. C. (2013). A reconstruction of regional and global temperature for the past 11,300 years. *Science*, *339*(6124), 1198–1201. https://doi.org/10.1126/science.1228026

Marsicek, J., Shuman, B. N., Bartlein, P. J., Shafer, S. L., & Brewer, S. (2018). Reconciling divergent trends and millennial variations in holocene temperatures. *Nature*, *554*(7690), 92–96. https://doi.org/10.1038/nature25464

Meko, D. & Touchan, R. & Anchukaitis, K.J., (2011). Seascorr: A MATLAB program for identifying the seasonal climate signal in an annual tree-ring time series. *Computers & Geosciences, 37*, 1234-1241. 10.1016/j.cageo.2011.01.013

Meulendyk, T., Moorman, B. J., Andrews, T. D., & MacKay, G. (2012). Morphology and development of ice patches in Northwest Territories, Canada. *ARCTIC, 65*(5). https://doi.org/10.14430/arctic4184

Mote, P. W., Li, S., Lettenmaier, D. P., Xiao, M., & Engel, R. (2018). Dramatic declines in snowpack in the western US. *Npj Climate and Atmospheric Science*, *1*(1). https://doi.org/10.1038/s41612-018-0012-1

Nguyen, D., & Widrow, B. (1990). Improving the learning speed of 2-layer neural networks by choosing initial values of the adaptive weights. *1990 IJCNN International Joint Conference on Neural Networks*. https://doi.org/10.1109/ijcnn.1990.137819

Pederson, G. T., Betancourt, J. L., & McCabe, G. J. (2013). Regional Patterns and proximal causes of the recent snowpack decline in the Rocky Mountains, U.S. *Geophysical Research Letters*, *40*(9), 1811–1816. https://doi.org/10.1002/grl.50424

Pederson, G. T., Gray, S. T., Ault, T., Marsh, W., Fagre, D. B., Bunn, A. G., Woodhouse, C. A., & Graumlich, L. J. (2011a). Climatic controls on the snowmelt hydrology of the northern Rocky Mountains. *Journal of Climate*, *24*(6), 1666–1687. https://doi.org/10.1175/2010jcli3729.1

Pederson, G. T., Gray, S. T., Woodhouse, C. A., Betancourt, J. L., Fagre, D. B., Littell, J. S., Watson, E., Luckman, B. H., & Graumlich, L. J. (2011b). The unusual nature of recent snowpack declines in the North American Cordillera. *Science*, *333*(6040), 332–335. https://doi.org/10.1126/science.1201570

Pilcher, J. R., Baillie, M. G., Schmidt, B., & Becker, B. (1984). A 7,272-year tree-ring chronology for Western Europe. *Nature*, *312*(5990), 150–152. https://doi.org/10.1038/312150a0

R Development Core Team. 2008. R: A Language and Environment for Statistical Computing. R Foundation for Statistical Computing, Vienna, Austria.

Reckin, R. (2013). Ice patch archaeology in global perspective: Archaeological discoveries from alpine ice patches worldwide and their relationship with paleoclimates. *Journal of World Prehistory*, *26*(4), 323–385. https://doi.org/10.1007/s10963-013-9068-3

Roig, F., Roig, C., Rabassa, J., & Boninsegna, J. (1996). Fuegian floating tree-ring chronology from subfossil Nothofagus Wood. *The Holocene*, *6*(4), 469–476. https://doi.org/10.1177/095968369600600410

Roig, F. A., Le-Quesne, C., Boninsegna, J. A., Briffa, K. R., Lara, A., Grudd, H., Jones, P. D., & Villagrán, C. (2001). Climate variability 50,000 years ago in mid-latitude Chile as reconstructed from tree rings. *Nature*, *410*(6828), 567–570. https://doi.org/10.1038/35069040

Salzer, M. W., Larson, E. R., Bunn, A. G., & Hughes, M. K. (2014). Changing climate response in near-treeline bristlecone pine with elevation and aspect. *Environmental Research Letters*, *9*(11), 114007. https://doi.org/10.1088/1748-9326/9/11/114007

Shuman, B.N., Serravezza, M., (2017). Patterns of hydroclimatic change in the Rocky Mountains and surrounding regions since the last glacial maximum. *Quaternary Science Reviews 173*, 58-77. https://doi.org/10.1016/j.quascirev.2017.08.012

Smith, W. K., Germino, M. J., Johnson, D. M., & Reinhardt, K. (2009). The altitude of Alpine Treeline: A bellwether of Climate Change Effects. *The Botanical Review, 75*(2), 163-190. https://doi.org/10.1007/s12229-009-9030-3

Stokes, M. A., & Smiley, T. L., (1996). An Introduction to Tree-Ring Dating. Tucson, AZ: The University of Arizona Press.

United States Department of Agriculture (USDA). Natural Resources Conservation Services. Snow Telemetry (SNOTEL) and Snow Course Data and Products. Available at. www.wcc.nrcs.usda.gov/snow. (Accessed January 2021).

Whitlock, C., Dean, W. E., Fritz, S. C., Stevens, L. R., Stone, J. R., Power, M. J., Rosenbaum, J. R., Pierce, K. L., & Bracht-Flyr, B. B. (2012). Holocene seasonal variability inferred from multiple proxy records from Crevice Lake, Yellowstone National Park, USA. *Palaeogeography, Palaeoclimatology, Palaeoecology*, *331-332*, 90–103. https://doi.org/10.1016/j.palaeo.2012.03.001

Wigley, T. M., Briffa, K. R., & Jones, P. D. (1984). On the average value of correlated time series, with applications in dendroclimatology and hydrometeorology. *Journal of Climate and Applied Meteorology*, *23*(2), 201–213. https://doi.org/10.1175/1520-0450(1984)023<0201:otavoc>2.0.co;2

Wise, E.K., Woodhouse, C.A., McCabe, G.J., Pederson, G.T., St-Jacques, J.M., (2018). Hydroclimatology of the Missouri river basin. *Journal of Hydrometeorolgy 19*, 161-182.

APPENDIX A

SUPPLEMENTARY DATA FOR CHAPTER 2 “A FOREST ENTOMBED IN ICE: A UNIQUE RECORD OF MID-HOLOCENE CLIMATE AND ECOSYSTEM CHANGE IN THE NORTHERN ROCKY MOUNTAINS, USA”

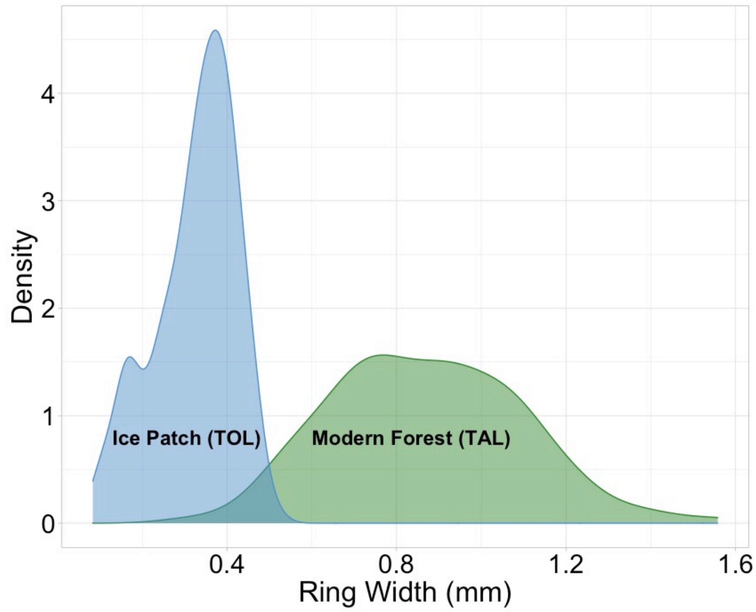

Figure S1. Kernel density plot showing the distribution of annual growth for the raw ring-width chronology (mm) from the modern upper treeline site (TAL) and the mid-Holocene Ice Patch site (TOL).

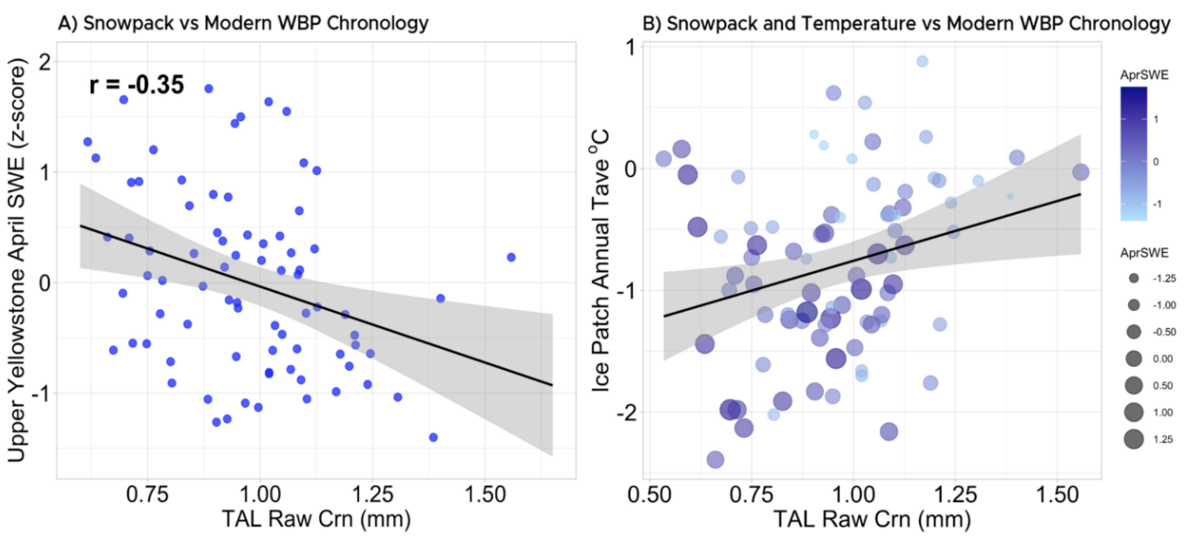

Figure S2. (*A*) Relationship between snowpack (measured as April 1 snow water equivalence; Upper Yellowstone April SWE) and modern whitebark pine tree growth (raw mm ring-widths). A negative linear relationship between snowpack and tree-ring-widths is shown (black line) and bracketed with 95% confidence intervals (gray shading). (*B*) Annual average temperature from the forest site is plotted with tree growth (raw ring-width chronology) along with snowpack (Upper Yellowstone April SWE; dot size and shading are scaled to represent snowpack anomalies). A positive linear relationship between annual average temperature and ring-width is shown (black line) and bracketed with 95% confidence intervals (gray shading). *Note*: While outliers exist, high snowpack tends to cluster in the lower left quadrant of the plot corresponding with lower temperatures and reduced tree-growth. Snow water equivalence data were obtained from basin-scale reconstructions derived from regional SNOTEL stations (Pederson et al., 2013; Pederson et al., 2011; Wise et al. 2018).

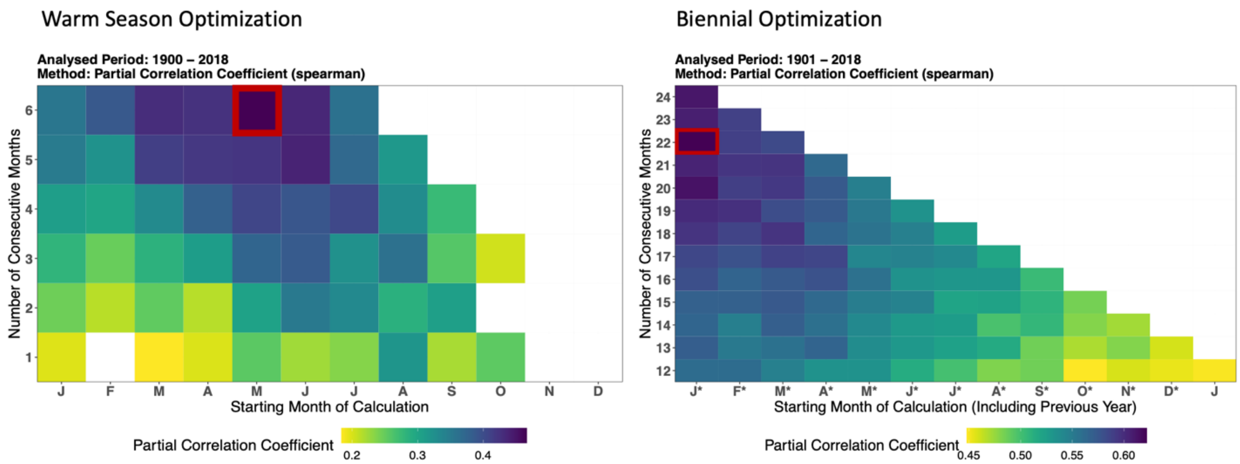

Figure S3. Spearman partial correlation coefficients of the optimized seasonal windows for annual average temperature (°C) and whitebark pine tree growth. *Left*: optimal 6-month warm-season (May-October) relationship. *Right*: optimal 22-month (previous January-current October) biennial relationship.

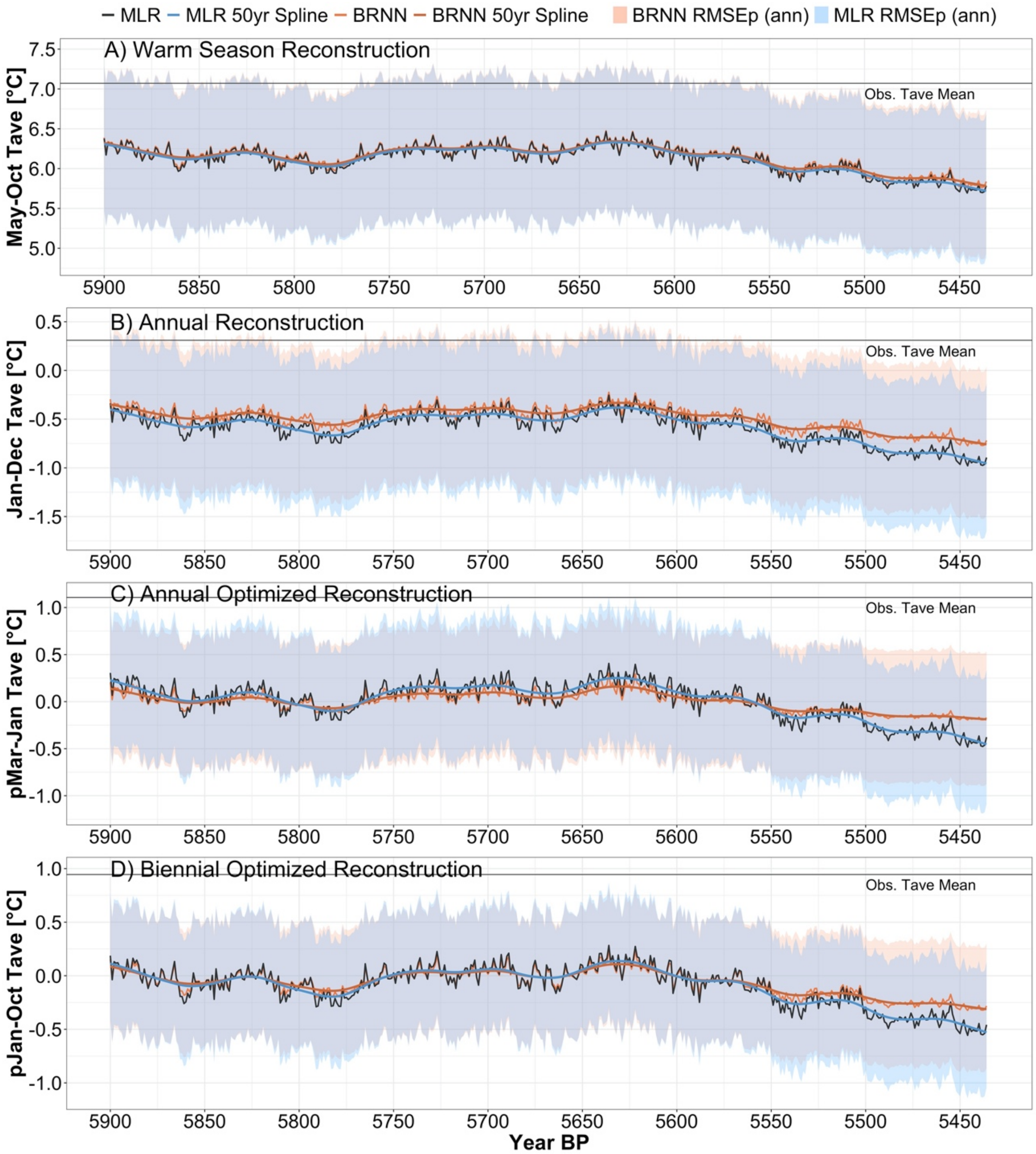

Figure S4. Temperature reconstructions from 5,900-5,436 year BP for the ice patch site derived from the relationship between modern whitebark pine tree growth and temperature. Reconstructions were developed using two methods: least-squares linear regression (MLR; light blue) and artificial neural networks with the Bayesian regularization training algorithm (BRNN; orange). *Note*: a 20th century mean line (black) for the forest site is shown for reference.

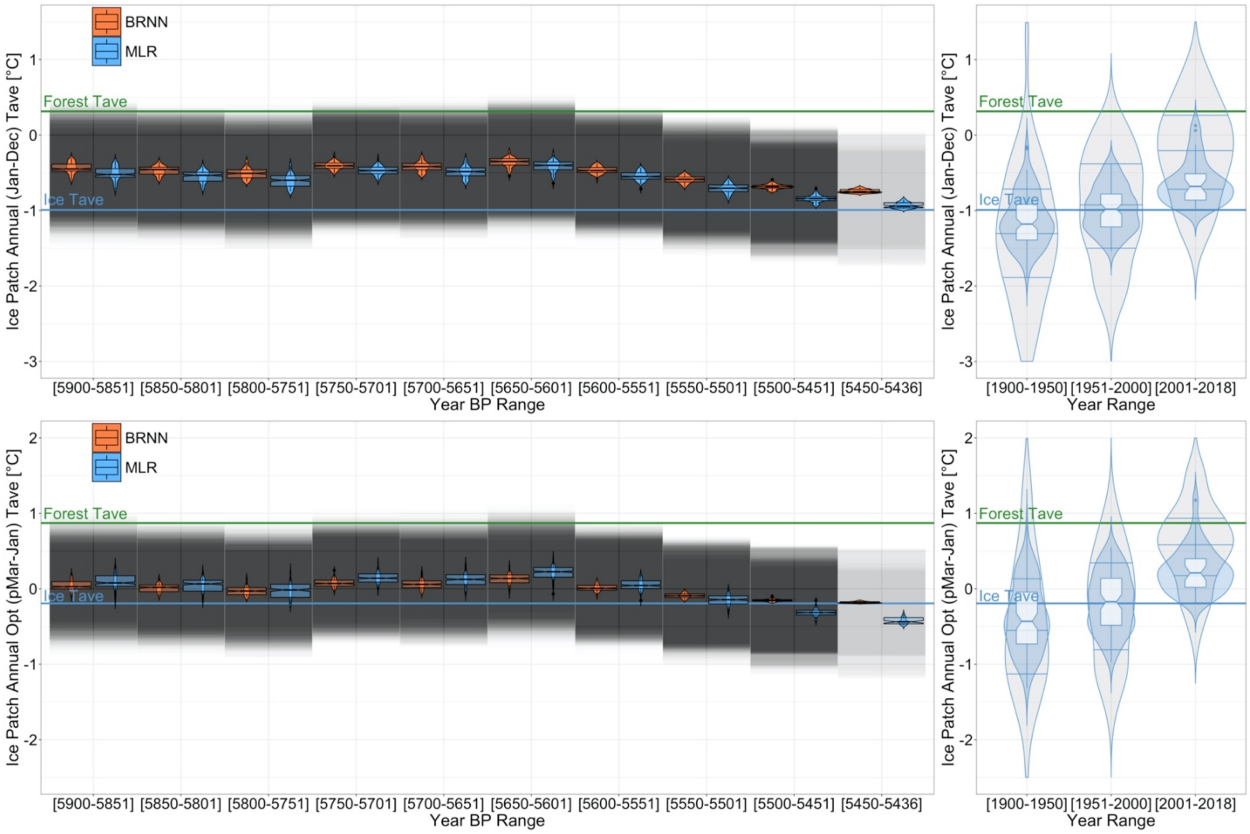

Figure S5. *Left*: 50-year bins of mid-Holocene temperature estimates (5,900-5,436 years BP) at the ice patch site derived using the MLR (light blue) and BNRR (orange) methods and bounded by the RMSE of the prediction (gray boxes) for the (non-optimized) annual reconstruction (top) and for the optimized annual reconstruction (bottom). *Right*: 50-year distribution of annual average temperatures (1900-2018) from the instrumental record (light gray violin plots) and temperature estimates from our reconstructions (blue violin plots). *Note*: present day temperatures at the ice patch (horizontal blue line) and at the upper treeline forest site (horizontal green line).

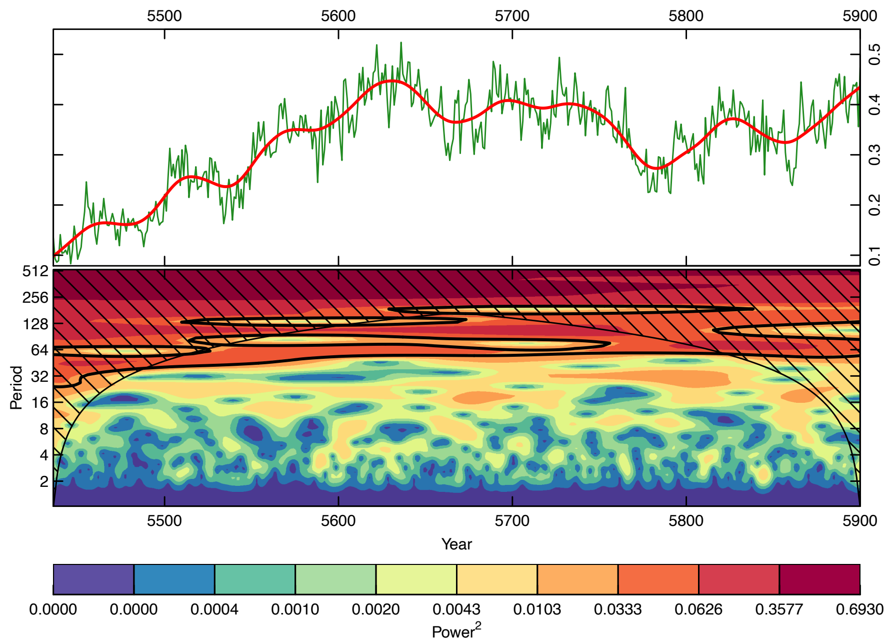

Figure S6. Wavelet analyses of the TOL subfossil WBP tree-ring chronology [5,900-5,436 (± 51.3) years BP]. Year (BP) is plotted along the x-axis and periodicity of the time series is plotted along the y-axis. Edge effects are constrained by the "cone of influence" (cross-hatched regions). There is minimal to no power indicated for sub-decadal periodicity that is typically associated with precipitation-sensitive chronologies (e.g., tree-ring chronologies sensitive to sub-decadal processes like El Niño-Southern Oscillation). Instead, the TOL subfossil chronology exhibits power at ~100-year frequencies, suggesting that long-term temperature variability is the dominant influence on stand wide tree-growth of the ancient forest.

Table S1. Least-squares linear regression models predicting mean temperature (°C) as a function of whitebark pine tree growth at the upper treeline site, fit across four seasonal windows: warm-season (May-Oct), annual (Jan-Dec), optimized 11-month annual (previous Mar through current Jan), and optimized biennial (previous Jan through current Oct).

Reconstruction Season	MLR Formula	d.f.	F	*p*-value	Durban-Watson Test*
Warm-season	May-Oct Tave = 5.548 + 1.749 x (TAL.raw)	117	21.852	<0.001	*DW* = 1.2791, *p*-value = 2.707e-05
Annual	Jan-Dec Tave = -1.115 + 1.643 x (TAL.raw)	117	27.481	<0.001	*DW* = 1.6919, *p*-value = 0.03894
Optimized Annual	pMar-Jan Tave = -0.649 + 2.015 x (TAL.raw)	116	46.696	<0.001	*DW* = 1.4434, *p*-value < 0.001
Optimized Biennial	pJan-Oct Tave = -0.649 + 2.015 x (TAL.raw)	116	60.363	<0.001	*DW* = 0.96946, *p*-value = 5.338e-09

Note: Durban Watson Test for significant autocorrelation remaining in model residuals.

Table S2. Optimization parameters for the Bayesian regularization training algorithm (BRNN).

Reconstruction Season	No. Parameters	Scaling Factor	Gamma	Alpha	Beta	w[1]	b[1]	Beta [1,1]
Warm-season	6	1.4	2.945	1.010	3.359	7.950	0.529	1.077
Annual	3	0.7	2.164	0.255	0.858	1.597	-0.728	1.078
Optimized Annual	3	0.7	2.706	0.193	0.998	2.093	-0.652	1.483
Optimized Biennial	3	0.7	2.697	0.739	5.415	1.986	-0.614	1.343

Note: A Bayesian regularized neural network (1-1-1 with 3 weights, biases and connection strengths). Inputs and output were not normalized. Training finished because: *Changes in F = beta*SCE + alpha*Ew in last 3 iterations less than 0.001.*

Table S3. Results from 10-fold cross-validation for the two methods utilized to develop seasonal temperature reconstructions: least-squares linear regression (*MLR*) and artificial neural networks with the Bayesian regularization training algorithm (*BRNN*). Seasonal windows for the temperature reconstruction are (A) warm-season [May-Oct], (B) annual [Jan-Dec], (C) annual optimized [previous Mar through current Jan], and (D) biennial optimized [previous Jan through current Oct].

Reconstruction Season	Metric	Period	BRNN (mean)	BRNN (std. dev)	MLR (mean)	MLR (std. dev)
Warm-season (May-Oct)	r	cal	0.395	0.038	0.396	0.030
	r	val	0.376	0.288	0.379	0.284
	RMSE	cal	0.902	0.020	0.901	0.020
	RMSE	val	0.904	0.175	0.902	0.176
	RRSE	cal	0.918	0.014	0.917	0.013
	RRSE	val	0.984	0.147	0.982	0.152
	d	cal	0.504	0.040	0.519	0.033
	d	val	0.494	0.124	0.507	0.131
	RE	val	0.125	0.217	0.127	0.227
	CE	val	0.011	0.322	0.014	0.332
Annual (Jan-Dec)	r	cal	0.282	0.215	0.289	0.226
	r	val	0.231	0.229	0.239	0.242
	RMSE	cal	0.180	0.243	0.189	0.257
	RMSE	val	0.129	0.257	0.139	0.273
	RRSE	cal	0.078	0.271	0.089	0.289
	RRSE	val	0.028	0.285	0.039	0.304
	d	cal	-0.023	0.299	-0.011	0.320
	d	val	-0.074	0.313	-0.061	0.336
	RE	val	-0.125	0.327	-0.111	0.351
	CE	val	-0.176	0.341	-0.161	0.367
Annual Optimized (prev. Mar-Jan)	r	cal	-0.227	0.355	-0.211	0.383
	r	val	-0.277	0.369	-0.261	0.398
	RMSE	cal	-0.328	0.383	-0.311	0.414
	RMSE	val	-0.379	0.397	-0.361	0.430
	RRSE	cal	-0.430	0.411	-0.411	0.445
	RRSE	val	-0.481	0.425	-0.461	0.461
	d	cal	-0.532	0.439	-0.511	0.477
	d	val	-0.582	0.453	-0.561	0.492
	RE	val	-0.633	0.467	-0.611	0.508
	CE	val	-0.684	0.481	-0.661	0.523
Biennial Optimized (prev. Jan-Oct)	r	cal	-0.735	0.495	-0.712	0.539
	r	val	-0.786	0.509	-0.762	0.555

Table S3 Continued

	RMSE	cal	-0.837	0.523	-0.812	0.570
	RMSE	val	-0.887	0.537	-0.862	0.586
	RRSE	cal	-0.938	0.551	-0.912	0.602
	RRSE	val	-0.989	0.565	-0.962	0.617
	d	cal	-1.040	0.579	-1.012	0.633
	d	val	-1.091	0.593	-1.062	0.649
	RE	val	-1.142	0.607	-1.112	0.664
	CE	val	-1.192	0.621	-1.162	0.680

Table S4. Results from central-edge test for the two methods utilized to develop seasonal temperature reconstructions: least-squares linear regression (*MLR*) and artificial neural networks with the Bayesian regularization training algorithm (*BRNN*). Seasonal windows for the temperature reconstruction are (A) warm-season [May-Oct], (B) annual [Jan-Dec], (C) annual optimized [previous Mar through current Jan], and (D) biennial optimized [previous Jan through current Oct].

Reconstruction Season	Metric	Period	BRNN	MLR
Warm-season (May-Oct)	r	cal_central	0.318	0.318
	r	val_edge	0.66	0.655
	RMSE	cal_central	0.895	0.895
	RMSE	val_edge	0.977	0.966
	RRSE	cal_central	0.948	0.948
	RRSE	val_edge	0.767	0.758
	d	cal_central	0.416	0.432
	d	val_edge	0.735	0.761
	RE	val_edge	0.416	0.429
	CE	val_edge	0.411	0.425
Annual (Jan-Dec)	r	cal_central	0.336	0.336
	r	val_edge	0.859	0.856
	RMSE	cal_central	0.78	0.779
	RMSE	val_edge	0.518	0.499
	RRSE	cal_central	0.942	0.942
	RRSE	val_edge	0.55	0.53
	d	cal_central	0.431	0.45
	d	val_edge	0.883	0.901
	RE	val_edge	0.697	0.72
	CE	val_edge	0.697	0.719
Annual Optimized (prev. Mar-Jan)	r	cal_central	0.552	0.54
	r	val_edge	0.653	0.635
	RMSE	cal_central	0.682	0.688
	RMSE	val_edge	0.804	0.934
	RRSE	cal_central	0.834	0.842
	RRSE	val_edge	0.787	0.914
	d	cal_central	0.675	0.666
	d	val_edge	0.809	0.789
	RE	val_edge	0.384	0.168
	CE	val_edge	0.381	0.164
Biennial Optimized (prev. Jan-Oct)	r	cal_central	0.568	0.56
	r	val_edge	0.738	0.719
	RMSE	cal_central	0.571	0.574
	RMSE	val_edge	0.672	0.738
	RRSE	cal_central	0.823	0.828

Table S4 Continued

	RRSE	val_edge	0.687	0.754
	d	cal_central	0.686	0.682
	d	val_edge	0.852	0.847
	RE	val_edge	0.529	0.432
	CE	val_edge	0.529	0.431